International Journal of Heat and Fluid Flow 77 (2019) 256–277

Contents lists available at ScienceDirect

International Journal of Heat and Fluid Flow

journal homepage: www.elsevier.com/locate/ijhff

Numerical analysis of the buckling and recuperation dynamics of flexible filament using an immersed boundary framework

Mithun Kanchan, Ranjith Maniyeri*

Biophysics Laboratory, Department of Mechanical Engineering, National Institute of Technology Karnataka (NITK), Surathkal, Mangalore, 575025, Karnataka, India

ARTICLE INFO

Keywords:
Diatom chains
Finite volume method
Immersed boundary method
Low Reynolds number
Viscous flow forcing
SIMPLE algorithm

ABSTRACT

The dynamics of flexible filaments in viscous shear flow is of interest to biologists and engineers in a wide variety of applications involving folding and unfolding sequence of long-chain biomolecules like DNA, non-motile sperm and microalgae. It is also helpful in understanding the deformation of natural and synthetic fibers which can be applied in areas such as biotechnology. In the present work, deformation and migration behavior of non-motile unicellular phytoplankton diatoms subjected to viscous shear flow are considered. These unicellular diatoms develop into colonies which are made up of linked chains. The complex fluid-structure interaction is solved by developing a two-dimensional numerical model with an immersed boundary framework. The simulation consists of suspending an elastic filament mimicking a diatom chain in a shear flow at low Reynolds number. The governing continuity and Navier–Stokes equations are solved on a Cartesian grid arranged in a staggered manner. A forcing term is added to the momentum equation that incorporates the presence of flexible filament in the fluid domain. The discretization of the governing equation is based on a finite volume method, and a SIMPLE algorithm is used to compute pressure and velocity. A computer code is developed to perform numerical simulations, and the model is first verified with the deformation study of a tethered flexible filament in uniform fluid flow. Next, the shape deformations for flexible filament placed freely in shear flow are compared with the studies of previous researchers. Further, the present results are validated with Jeffery's equation for particles immersed in shear flow along with classification plot for filament orbit regimes. All of these comparisons provide a reasonable validity for the developed model. The effect of bending rigidity and shear rate on the deformation and migration characteristics is ascertained with the help of parametric studies. A non-dimensional parameter called Viscous Flow Forcing value (VFF) is calculated to quantify the parametric results. An optimum Viscous Flow Forcing value is determined which indicates the transition of filaments exhibiting either a recuperative (regaining original shape past deformation) or non-recuperative (permanently deformed) behavior. The developed model is successful in capturing fluid motion, diatom buckling, shape recurrences and recuperation dynamics of diatom chains subjected to shear flow. Further, the developed computational model can successfully illustrate filament-fluid interaction for a wide variety of similar problems.

1. Introduction

Fluid-structure interaction (FSI) comprises a large number of problems in the field of biofluid dynamics and biophysics. Flow interaction between blood and heart-valve leaflets, motion, and deformation of red blood cells, bundling and tumbling of the bacterial flagellum, sperm motility, swimming fish, etc. are some of the commonly known examples. An excellent example of elastic fibers which undergo stretching, compression and bending in moving fluids are DNA, diatom chains and actin fibers. To understand the hydrodynamics and factors causing the fibers to behave recuperatively or non-recuperatively in an incompressible viscous fluid is very important for a wide range of medical and engineering applications.

The impact of oceanic fluid motion on solute transport to micro-organisms is fundamental to marine ecology. Of particular interest is the FSI of a group of diatoms, non-motile unicellular phytoplankton which forms the primary foundation of aquatic food webs. While it is unicellular, the micro-organism has developed the ability to form colonies as chains linked together. The phytoplankton lives in these chains whose size vary from 5 micrometers to a few millimeters (Guasto et al., 2012). The mechanical properties of these chains change according to morphology and linking structure material. The diatoms are also photosynthetic micro-organisms which require dissolved nutrients in the form of nitrates, phosphates, etc., delivered to the surface of its

* Corresponding author.
E-mail address: mranji1@nitk.edu.in (R. Maniyeri).

https://doi.org/10.1016/j.ijheatfluidflow.2019.04.011
Received 20 December 2018; Received in revised form 25 March 2019; Accepted 22 April 2019

cells by fluid motion. The ability of the diatoms to uptake nutrients depends on its interaction with surrounding fluid thus highlighting that ambient fluid motion is crucial for survival. The functional role of hydrodynamics on chain deformation and migration has not been clearly understood. The study thus falls under the purview of filament-fluid interaction. To describe the physics adequately and develop numerical models for such interactions is a significant challenge because it consists of the complex interplay between filament conformity and hydrodynamic stresses induced by the fluid. However, in the last few years, researchers have successfully captured the interaction of flexible filaments in a viscous fluid with the help of numerous methods and techniques supported by experimental studies.

An early study by Jeffery (Jeffery, 1922) provided a mathematical understanding for the motion of a single rigid elliptical particle in shear flow. The analysis of these idealized ellipsoids was successfully approximated to describe the behavior of rigid cylindrical filaments. However, the same was not applicable to flexible filaments. Flexible fibers exhibit a rich range of motions when subjected to background shear flow. This was experimentally observed by Forgacs et al. (Forgacs and Mason, 1959), who categorized filament deformation into various orbit classes. The orbits included deformation involving snake turns, “S” turns and complex coiling phenomena. They demonstrated that hydrodynamic drag forces and fiber bending forces play a critical part in filament shape transitions. Bead-rod model was used to simulate flexible filaments in which rigid beads were linked by elastic connectors (Yamamoto and Matsuoka, 1993). It was further extended by Ross et al. (Ross and Klingenberg, 1997) who studied the suspension and flow dynamics of rigid and flexible filaments by performing a particle-level simulation with the filament made up of linked rigid prolate spheroids. The simulation reasonably demonstrated Jeffery orbits for rigid fibers and experimental works of Forgacs et al. (Forgacs and Mason, 1959) for flexible filaments. Lindstrom et al. (Lindström and Uesaka, 2009; Lindström and Uesaka, 2007) modified bead-rod model to simulate rigid and flexible fibers by using the Navier–Stokes equation as the fluid governing equation. When considering numerical studies involving single bio-polymers like actin filament and microtubules, continuum formulation techniques such as slender-body theory (SBT) (Batchelor, 1970) have been quite popular. They are easy to implement but fail to capture far-field fluid motion accurately. To address this problem, Keller et al. (Keller and Rubinow, 1976) developed a non-local SBT that captures the global effect on the fluid velocity arising from the presence of the filament, making use of the theory of fundamental solutions for Stokes flow. Shelley et al. (Shelley and Ueda, 2000) also developed a numerical method based on a non-local SBT for simulating flexible filaments. Their interest was in understanding the dynamics of growing and buckling flexible filament, motivated by observations of phase transitions in smectic-A liquid crystals. Tornberg et al. (Tornberg and Shelley, 2004) employed non-local SBT to study dynamics of slender filaments in Stokesian fluids. An integral equation is developed which relates the force exerted on the body with the filament velocity. The simulations show shear-induced buckling in filaments which are a characteristic property of visco-elastic fluids that are suspended as microscopic elastic fibers. However, the above method becomes invalid when considering multiple elastic members in close vicinity, which was overcome by regularized Stokeslets method (Bouzarth et al., 2011). A kinetic theory dumbbell model was developed by Jandrejack et al. (Jendrejack et al., 2004), to simulate flexible polymers keeping DNA as a reference molecule. It was found that flow strength was fundamental in stretching and deforming highly confined DNA chains from its equilibrium position. Also, the DNA chains migrate back to channel centerline in agreement with experimental studies. Slowicka et al. (Słowicka et al., 2015) studied the fiber dynamics in shear flow for different values of bending rigidity. A bead-spring model based multi-pole method was used to simulate fiber dynamics for a wide range of applications involving DNA, polymers, proteins, and biological macromolecules. The work emphasized the importance of using a non-dimensional number which is the ratio of fiber bending force to viscous drag force and thus categorized fiber deformation to bending rigidity. Depending on the selected bending rigidity and resulting hydrodynamic interactions, fibers were grouped into either behaving rigid or flexible. They also observed that fibers with high stiffness placed in shear flow, later stay in a plane perpendicular to shear gradient and at an angle to vorticity direction for a large portion of simulation time. They found rigid fibers tending to straighten out and flexible fibers coil thus indicating distinct evolution patterns for rigid and flexible fibers. In the majority of these studies, the hydrodynamic interactions were neglected thus providing limited information of the underlying FSI. The coupling between the structure and fluid is one-way, i.e., fluid was considered as a passive medium, and the fiber did not exert any force back onto the fluid. The computational complexity may reduce significantly, but they cannot effectively elucidate deformation and mobility of bio-molecules subjected to hydrodynamic stresses due to surrounding fluid motion, as compared to grid-based methods. A brief discussion on grid-based simulation is provided below.

In understanding FSI, it is always convenient to describe the fluid region as a Eulerian frame of reference and the solid region as a Lagrangian formulation. Meshing techniques in FSI can be grouped into body-fitted/conformal methods and non-conformal methods. Body-fitted methods consist of widely known Arbitrary Lagrangian–Eulerian formulation (ALE) (Hu et al., 2001) which use the finite element method (FEM). For complex geometries, however, the quality of the grid may deteriorate since the mesh has to adapt to the moving boundaries and an iterative grid refinement algorithm may be required to prevent convergence failure. Among the non-body-fitted techniques, the immersed boundary method (IBM) developed by Peskin (Peskin, 2002) is quite popular. The method was originally used to simulate cardio-mechanism and has been successfully implemented to simulate complex biofluid dynamic problems. Examples include propulsion of bacterial flagella (Maniyeri et al., 2012), elastic rod dynamics in viscous fluid (Maniyeri and Kang, 2012), flexible fiber suspension in shear flow (Stockie and Green, 1998), inertial migration of elastic capsule (Kim et al., 2015), Pleurobrachia and cilia propulsion (Dauptain et al., 2008), valveless pumping (Shin et al., 2012), droplet dynamics in shear flow (Hua et al., 2014), flapping filaments (Zhu and Peskin, 2002), flexible propulsor (Kim et al., 2017), inverted flags (Ryu et al., 2018) and flexible fin (Kim et al., 2016). The characteristic feature about this method is that it consists of a non-conforming mesh with a monolithic flow structure solver. The absence of grid transformation terms significantly reduces per-grid-point operation count (Mittal and Iaccarino, 2005). It is also very well suited for moving boundary problems. The fluid is solved on a Cartesian grid system, and structure is discretized on connected Lagrangian markers to capture its elastic response relative to fluid motion. The calculated elastic forces are then distributed to the background Cartesian grid covering the fluid volume utilizing momentum forcing, eventually modifying the fluid flow near the structure. This coupling between Eulerian and Lagrangian variables is carried out by Dirac delta function. Since its inception by Peskin, numerous modifications and refinements have been carried out by researchers with respect to application requirements. Numerical studies based on IBM for filament-fluid interaction are presented below.

Stockie (Stockie, 2002) simulated a single three-dimensional wood pulp fiber in shear flow, to understand the behavior of long, flexible filament which is in suspension. This work was an extension of the previously developed two-dimensional model (Stockie and Green, 1998). The pulp fiber model is made up of several layers of cellulose fibrils, interwoven to form a complex network, making up the wood cell. The linking elements were made up of springs which resist stretching and bending forces. This gives a more realistic and detailed representation of the fiber model. Weins et al. (Wiens and Stockie, 2015) had successfully recreated two-dimensional orbit classes for flexible filaments suspended in a viscous fluid using the immersed boundary method. A pseudo-compressible fluid solver was used, and

filaments were modeled as Kirchhoff rod. Nguyen et al. (Nguyen and Fauci, 2014) studied the hydrodynamics of diatom chains and flexible fibers in three-dimensions using an adaptive grid-based immersed boundary method. They were successful in capturing recuperation and buckling dynamics for a wide range of diatom species. In order to capture the full fluid motion around the fiber, the fluid grid has to be refined. More recently, Kunhappan et al. (Kunhappan et al., 2017) studied the dynamics of high aspect ratio flexible fibers in an inertial flow by coupling discrete element method and finite volume method. The simulation was three-dimensional and contained an unstructured grid scheme. Such three-dimensional models are complex and very expensive. A two-dimensional model on the other hand effectively predicts dynamics of flexible filament and also reduces the computational expense. In this direction, Musielak et al. (Musielak et al., 2009) had studied the role of fluid motion on nutrient uptake in diatoms using a two-dimensional immersed boundary method. The study focused on understanding nutrient uptake and diatom behavior for different filament lengths and bending rigidity. Diatoms were made up of linked chains, and the one behaving rigid tend to experience high nutrition gradients as compared to flexible diatoms. However, at that time no laboratory measurements of bending rigidity were reported for diatom chains. As a result, a direct relationship between the modeled diatoms and its experimental counterpart could not be accurately assessed. Young et al. (Young et al., 2012) experimentally quantified the bending rigidity for various types of diatom chains. The diatoms were suspended in a medium of seawater and exposed to hydrodynamic forces across a hollow capillary tube. They analyzed the response of the diatoms to the applied force, and thus a measure of its bending ability was determined. By studying the deformation of the filament and measuring the chain dimensions, the flexural rigidity of different diatom chains was experimentally obtained by them. Numerical studies of Slowicka et al. (Słowicka et al., 2015) and Musielak et al. (Musielak et al., 2009) have thus shown that fiber dynamics largely depends on flow strength, bending rigidity and fiber length respectively. Hence it can be seen that a two-dimensional numerical study can accurately predict the behavior of diatom chains subjected to shear flow at lower computational costs. Studies by Lazier et al. (Lazier and Mann, 1989) had indicated that since diatom chains are typically smaller than the Kolmogorov length scales in the ocean, they experience turbulence as linear shear. Jumars et al. (Jumars et al., 2009) also suggested the importance of background flows leading to the formation of dissipative vortices around diatom structures. Thus, we can ascertain from the above literature reviews that, very few studies have reported and quantified transition of filaments from recuperative to non-recuperative behavior especially for the case of diatom chains and thus parametric study is essential in this direction. Quantitative information like bending rigidity obtained from the experimental values of Young et al. (Young et al., 2012) was not used in two-dimensional diatom simulations by previous researchers. Three-dimensional simulations and adaptive mesh refinement techniques (Vanella et al., 2014) have high computational costs and thus have hindered design and dynamic coupling of more mechanically realistic diatom model with an incompressible fluid. A point to be noted in this regard is that the two-dimensional model can never possibly capture the full fluid dynamics as compared to three-dimensional one. However, capturing the essential and prominent fluid motion and filament deformation characteristics using a simplified model of diatom chains with minimum mesh generation overhead outweighs the drawback of costly computations. Also, very few studies have captured fluid motion in the vicinity of the filament which is essential for understanding the hydrodynamic interactions over successive time periods. Through the present work, an attempt is made to capture and visualize dissipative vortices formed in the vicinity of diatom chains to understand how such vortices are formed and what advantages the organism can achieve to nutrient uptake. This will help to realize the underlying mechanism responsible for shape formations and transitions observed during deformation of rigid and flexible filaments. Finally, there is a need to capture the migratory behavior of filaments in order to understand its behavior to external factors better. These shortcomings from previous works are the real motivation for the present problem.

In the present work, a two-dimensional numerical model based on an immersed boundary method is developed to capture the hydrodynamic interaction of rigid and flexible filaments in shear flow. A parametric analysis is carried out by varying filament length, bending rigidity and shear rate. The numerical method incorporated in this study is provided in Section II. The simulation results and details regarding filament deformation and migration are provided in Section III. Finally, the conclusions are deduced in Section IV.

2. Mathematical framework and numerical procedure

The physics of the problem involves a flexible filament which is massless and neutrally buoyant, suspended in a viscous incompressible fluid medium. The Cartesian co-ordinates $\mathbf{x}^* = (x^*, y^*)$ are the Eulerian variables used to define the fluid flow. A Lagrangian frame of reference is used to define the filament displacement, given by a curvilinear material co-ordinate s^* and time t^*. The flow variables are velocity $\mathbf{u}^*$ ($\mathbf{x}^*$, t^*), pressure p^* ($\mathbf{x}^*$, t^*) and Eulerian force density $\mathbf{f}^*$ ($\mathbf{x}^*$, t^*). The filament position $\mathbf{X}^*$ (s^*, t^*), filament velocity $\mathbf{U}^*$ (s^*, t^*) and Lagrangian force density $\mathbf{F}^*$ (s^*, t^*) are the filament variables. The shear flow is developed by moving the top and bottom walls horizontally. The top and bottom wall move in positive and negative x-direction respectively with a constant speed $\mathbf{U}^*_{\mathbf{wall}}$. In the absence of filament, a linear shear flow is developed with velocity profile given by Eq. (1).

$$\mathbf{u}^* = G^*\left(y^* - \frac{H^*}{2}\right) \tag{1}$$

where, $G^* = \frac{2U^*_{wall}}{H^*}$ is the shear rate and H^* is the height of the channel. The equation of motion for fluid flow and filament are given below.

$$\rho\frac{\partial \mathbf{u}^*}{\partial t^*} + \mathbf{u}^*\cdot\nabla^*\mathbf{u}^* = -\nabla^* p^* + \mu\nabla^{*2}\mathbf{u}^* + \mathbf{f}^*(\mathbf{x}^*, t^*) \tag{2}$$

$$\nabla^* \cdot \mathbf{u}^* = 0 \tag{3}$$

where, the constant μ is the fluid viscosity and ρ the fluid density. Eq. (2) and Eq. (3) are the incompressible Navier–Stokes equation and continuity equation with a momentum forcing term. They can be non-dimensionalized based on the following characteristic scales: the length of the filament as the reference length L_{ref}, constant velocity of moving walls as U_{ref}, time scale t_{ref} as L_{ref} / U_{ref}, shear rate G_{ref} as U_{ref} / L_{ref}, pressure p_{ref} as ρU^2_{ref}, momentum forcing f_{ref} as ρU^2_{ref} / L_{ref} and bending stiffness as $\rho U^2_{ref} L^3_{ref}$.

The resulting non-dimensionalized equations are given as,

$$\frac{\partial \mathbf{u}}{\partial t} + \mathbf{u}\cdot\nabla\mathbf{u} = -\nabla p + \frac{1}{Re}\nabla^2\mathbf{u} + \mathbf{f}(\mathbf{x}, t) \tag{4}$$

$$\nabla \cdot \mathbf{u} = 0 \tag{5}$$

where, $Re = \frac{\rho u_{ref} L_{ref}}{\mu}$

The flexible filament is made up of a number of Lagrangian points connected together by means of resistance links having resting length Δs. The Lagrangian force $\mathbf{F}$ acting on immersed boundary points and produced by the filament motion are spread to the fluid domain, and a momentum force term $\mathbf{f}$ is calculated which in turn drives fluid motion. The Lagrangian force $\mathbf{F}$ consisting of stretching/compression, and bending forces is shown in Eq. (6) as,

$$\mathbf{F}(s, t) = \frac{\partial E_s}{\partial X} + \frac{\partial E_b}{\partial X} \tag{6}$$

where, E_s is the elastic energy derived from Hooke's Law given in Eq. (7), and E_b is the bending energy obtained from the principle of least action given in Eq. (8). The energy equations are taken from the numerical works of Zhu et al. (Zhu and Peskin, 2002). An illustration of

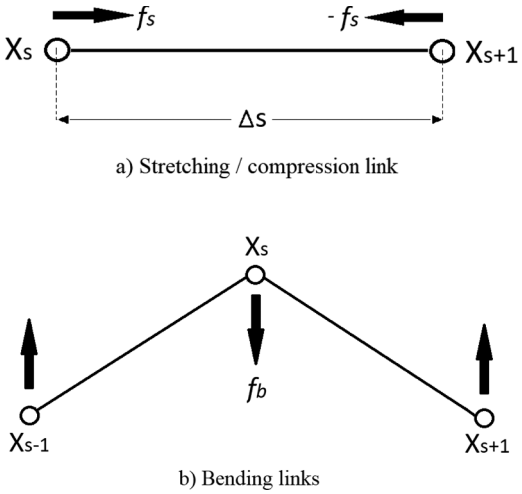

Fig. 1. The two types of filament linkages used in the present study. a) Stretching/compression resistance linkage and b) Bending resistance linkage between Lagrangian points.

the resultant stretching and bending forces acting on the linkages are provided in Fig. 1(a) and Fig. 1(b) respectively. In the figure, X_s is the Lagrangian point surrounded by nearby points X_{s+1} and X_{s-1}.

$$E_s = \frac{1}{2} K_s \int \left(\left| \frac{\partial \mathbf{X}}{\partial s} \right| - 1 \right)^2 ds \tag{7}$$

$$E_b = \frac{1}{2} K_b \int \left| \frac{\partial^2 \mathbf{X}}{\partial s^2} \right|^2 ds \tag{8}$$

In Eq. (7) and Eq. (8), K_s and K_b are the stretching co-efficient and bending co-efficient of the filament respectively. From the above equations, the Lagrangian force **F** is determined. This term is then substituted in Eq. (9) to calculate momentum force term **f** given as,

$$\mathbf{f}(\mathbf{x},\ t) = \int \mathbf{F}(s,\ t)\delta(\mathbf{x} - \mathbf{X}(s,\ t))ds \tag{9}$$

where, δ_h is the two-dimensional Dirac delta function. In our formulation δ_h is chosen such that,

$$\delta_h(\mathbf{x}) = \frac{1}{h^2}\phi\left(\frac{x}{h}\right)\phi\left(\frac{y}{h}\right) \tag{10}$$

where, h is the Eulerian mesh width and ϕ is given by,

$$\phi(r) = \begin{cases} \frac{1}{4}\left(1 + \cos\left(\frac{\pi r}{2}\right)\right), & if\ |r| \le 2, \\ 0, & otherwise \end{cases} \tag{11}$$

The Dirac delta function (Eq. (11)) in the present study is chosen based upon the numerical works of Maniyeri et al. (Maniyeri et al., 2012; Maniyeri and Kang, 2014). By substituting the calculated momentum force term in Eq. (4), we obtain new fluid velocity at the next time step. According to the newly calculated fluid velocity, the filament velocity is determined which is given by Eq. (12). Finally, the new position of the filament is computed from Eq. (13).

$$\mathbf{U}(s,\ t) = \int \mathbf{u}(\mathbf{x},\ t)\delta_h(\mathbf{x} - \mathbf{X}(s,\ t))dx \tag{12}$$

$$\frac{\partial \mathbf{X}}{\partial t}(s,\ t) = \mathbf{U}(s,\ t) \tag{13}$$

The numerical method of the present study is formally second-order. Using a formally second-order scheme makes it possible to obtain results with better accuracy (Lai and Peskin, 2000). The total time step is divided into two stages. One is the preliminary stage, and the other is the final stage. In the preliminary stage, the governing equations are solved for time level $(n + \frac{1}{2})$ from data available at time level n using an accurate first-order scheme. The results of the preliminary stage are used to proceed in the final stage to reach time level $(n + 1)$ in a formally second-order manner. If Δt is the time step, the fluid velocity for present time n is depicted as $\mathbf{u^n}$ while boundary configuration is $\mathbf{X^n}$. The objective of the numerical procedure is to compute updated $\mathbf{u^{n+1}}$ and $\mathbf{X^{n+1}}$ using the data given at time level n. Now starting the numerical procedure, the preliminary stage from time level n to level $(n + \frac{1}{2})$ is initiated, and the boundary configuration is updated to a new position $\mathbf{X^{(n\ +\ 1)/2}}$ by discretizing Eq. (13) as,

$$\frac{\mathbf{X}^{(n+1)/2} - \mathbf{X}^n}{\left(\frac{\Delta t}{2}\right)} = \sum_{\mathbf{x}} \mathbf{u}^n(x)\delta_h(x - \mathbf{X}^n(s,\ t))h^2 \tag{14}$$

Next, the Lagrangian force density $\mathbf{F}^{(n+1)/2}$ which consists of elastic forces acting on immersed boundary points is discretized and calculated as,

$$\mathbf{F}^{(n+1)/2} = -\frac{\partial E[\mathbf{X}^{(n+1)/2}]}{\partial \mathbf{X}} \tag{15}$$

The force density term $\mathbf{F^{(n\ +\ 1)/2}}$ calculated at IB points are further converted to momentum forcing term $\mathbf{f}^{(n\ +\ 1)/2}$ at Cartesian grid points to be applied in the governing Navier–Stokes equations. The discretized form of momentum forcing term $\mathbf{f}^{(n\ +\ 1)/2}$ is given as,

$$\mathbf{f}^{(n+1)/2} = \sum_{\mathbf{s}} \mathbf{F}^{(n+1)/2}(s)\delta_h(x - \mathbf{X}^{(n+1)/2}(s,\ t))\Delta s \tag{16}$$

With the newly calculated $\mathbf{f^{(n\ +\ 1)/2}}$, Eq. (4) and Eq. (5) can be discretized and solved as

$$\frac{\mathbf{u}^{(n+1)/2} - \mathbf{u}^n}{\left(\frac{\Delta t}{2}\right)} = -\nabla p^{(n+1)/2} - [\mathbf{u}\cdot\nabla\mathbf{u}]^{(n+1)/2} + \frac{1}{Re}\nabla^2\mathbf{u}^{(n+1)/2} + \mathbf{f}^{(n+1)/2} \tag{17}$$

$$[\nabla\ .\ \mathbf{u}]^{(n+1)/2} = 0 \tag{18}$$

This concludes the preliminary stage. The final stage is started again at time level n to reach level $(n + 1)$ using intermediate variables $\mathbf{u^{(n\ +\ 1)/2}}$ and $\mathbf{X^{(n\ +\ 1)/2}}$ obtained from the preliminary stage.

First, the boundary configuration $\mathbf{X^{n+1}}$ is calculated as,

$$\frac{\mathbf{X}^{n+1} - \mathbf{X}^n}{\Delta t} = \sum_{\mathbf{x}} \mathbf{u}^{(n+1)/2}(x)\delta_h(x - \mathbf{X}^{(n+1)/2}(s,\ t))h^2 \tag{19}$$

Next, the Lagrangian force density $\mathbf{F^{n+1}}$ and momentum forcing term $\mathbf{f^{n+1}}$ are calculated from discretized Eq. (20) and Eq. (21) respectively.

$$\mathbf{F}^{n+1} = -\frac{\partial E[\mathbf{X}^{n+1}]}{\partial \mathbf{X}} \tag{20}$$

$$\mathbf{f}^{n+1} = \sum_{\mathbf{s}} \mathbf{F}^{n+1}(s)\delta_h(x - \mathbf{X}^{n+1}(s,\ t))\Delta s \tag{21}$$

Finally, the fluid velocity $\mathbf{u^{(n\ +\ 1)/2}}$ is updated to new time $(n + 1)$ marking the end of final stage.

$$\frac{\mathbf{u}^{n+1} - \mathbf{u}^n}{\Delta t} = -\nabla p^{n+1} - [\mathbf{u}\cdot\nabla\mathbf{u}]^{n+1} + \frac{1}{Re}\nabla^2\mathbf{u}^{n+1} + \mathbf{f}^{n+1} \tag{22}$$

$$[\nabla\ .\ \mathbf{u}]^{n+1} = 0 \tag{23}$$

Thus, the present numerical immersed boundary scheme completes a typical time step Δt. The fluid Cartesian grid is arranged in a staggered manner, and the flow variables are solved using an implicit time advancement scheme based on Finite volume method (FVM). The method of deferred correction is used to treat the convective and diffusive fluxes obtained from the finite-volume discretization of the Navier–Stokes equation. Hayase et al. (Hayase et al., 1992) had described this scheme to discretize systems having oscillatory solutions and for maintaining the diagonal dominance. The source term is modified to contain the difference between the first-order upwind scheme and central

differencing. The spatial derivatives are discretized using a second-order difference scheme. The continuity and momentum equations are solved using a SIMPLE algorithm. The technique involves an iterative procedure with pressure correction. A pressure value is guessed, and an intermediate velocity is first calculated which is used as input to the pressure Poisson equation. The ICCG (Incomplete Cholesky Conjugate Gradient) method is used to solve the pressure equation. The newly calculated pressure is used to determine the fluid velocity at the new time step thus keeping the solution divergent free. The new fluid velocity is used and the deformation of filament for different time steps is captured. A periodic boundary condition is applied in the positive x-direction with flow driven by a constant pressure gradient. A dimensionless parameter called Viscous Flow Forcing value (VFF) is used to quantify viscous drag effects of the fluid with respect to filament elastic forces which is given in Eq. (24) as,

$$\mathrm{VFF} = \frac{\mu G^*(L^*)^3}{EI} \tag{24}$$

where, E is Young's modulus of filament material, and I is the moment of area in the bending plane. The Viscous Flow Forcing value is related to the viscosity of the fluid, length of the filament, shear rate and bending rigidity of the filament. The use of a similar parameter where reported in the works of (Ross and Klingenberg, 1997; Stockie and Green, 1998; Stockie, 2002; Wiens and Stockie, 2015; Nguyen and Fauci, 2014; Liu et al., 2018).

3. Results and discussion

3.1. Model validation

The numerical model described in the previous section is compared with filament deformation problem done by Vahidkhah et al. (Vahidkhah and Abdollahi, 2012) who performed two-dimensional numerical simulation using an immersed boundary-lattice Boltzmann method. The deformation problem involves a massless flexible filament placed in a rectangular channel and subjected to uniform Poiseuille flow. The fluid is viscous and incompressible while the filament is placed horizontally with an inclination of $\Theta = 45^{\circ}$ The dimensionless length of channel (L_c) and height of the channel (H) are taken as 4.0 and 1.0 respectively. The length of the filament (L) is 0.43, and the leading edge is fixed at the location $L_1 = 1.0$ and $H/2 = 0.5$, while the trailing edge is free to move along the fluid flow direction. No-slip boundary condition is applied to the top and bottom channel walls. A Periodic boundary condition is applied in the positive x-direction with the flow being driven by a constant pressure gradient. A schematic representation of the problem and the boundary condition applied is provided in Fig. 2. The Reynolds number chosen for this study is 1.0 and the total simulation time is 1.0.

Table 1
Comparison of% inextensible error (ε) for varying time step (Δt) and varying stretching co-efficient (K_s) for fixed value of bending co-efficient ($K_b = 1.0$).

Stretching co-efficient (K_s)	Time step (Δt)	% Inextensible error (ε)
1000	1.0×10^{-4}	7.35
5000	1.0×10^{-5}	1.86
7500	1.0×10^{-5}	2.64
10,000	1.0×10^{-5}	2.95

Before considering the solution to the problem, the inextensible property of the filament is tested for varying time step Δt and stretching co-efficient K_s for fixed bending co-efficient K_b. This serves as a stability analysis for our numerical model. Next, the spatial convergence of the model is analyzed by considering different Eulerian grids in x and y-directions. The objective of these two tests is to obtain a divergence free and accurate solution to the filament deformation study. In order to perform the inextensible test, % inextensible error (ε) is used which calculates the deviation from the original filament length. This is given in Eq. (25).

$$\varepsilon(t) = \max\left|\frac{\partial \mathbf{X}}{\partial s}.\frac{\partial \mathbf{X}}{\partial s} - 1\right| \times 100 \tag{25}$$

The inextensible error equation is taken from simulation study of flexible filament in uniform flow by Huang et al. (Huang et al., 2007). Their methodology strictly enforces the filament inextensibility condition with no restrictions on time step. Table 1 shows different cases that are analyzed by varying time step and stretching co-efficient for fixed bending co-efficient of $K_b = 1.0$. The filament cannot resist the fluid forces at low stretching co-efficient ($K_s = 1000$), thus producing a large % inextensible error of 7.35. There is a need to increase the stretching co-efficient in order to keep the filament in-extensible. However, the time step needs to be reduced to 1×10^{-5} in order to minimize the effect of oscillations in the solution caused by incorporating higher stretching co-efficient as observed in Table 1. Increasing stretching co-efficient reduces% inextensible error and the best value of stretching co-efficient ($K_s = 5000$) produces the least% error of 1.86. Filaments with stretching co-efficient greater than 5000 tend to develop an initial compression state between time $t = 0.0$ to $t = 0.15$. This factor significantly increases the% error for cases of higher stretching co-efficient.

Regarding filament inextensibility, the spatial convergence test for

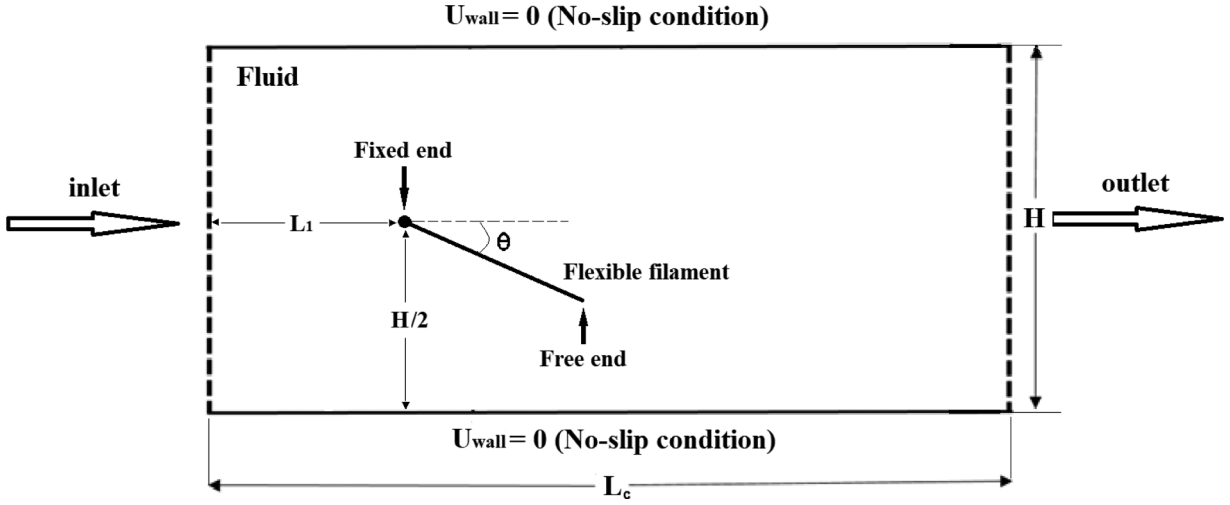

Fig. 2. Schematic illustration of flexible filament placed at a channel location in the direction of viscous fluid flow.

Table 2
Comparison of% inextensible error (ε) with different uniform Eulerian grids in x and y-direction.

Grids	Time step (Δt)	% Inextensible error (ε)
256 × 64	1.0×10^{-5}	5.26
512 × 128	1.0×10^{-5}	1.86
1024 × 256	1.0×10^{-5}	1.82

different Eulerian grids is carried out. A uniform grid is considered for all cases and compared with% inextensible error as seen in Table 2. It is clear from Table 2 that the best possible grid configuration is 512 × 128.

Based on inextensibility and grid convergence tests, two-dimensional numerical simulation of inclined flexible filament placed in a uniform flow is carried out. The filament deformation for different time instances is provided in Fig. 3a–Fig. 3d. The filament which is initially inclined shown in Fig. 3a aligns itself with the flow direction. Finally, at

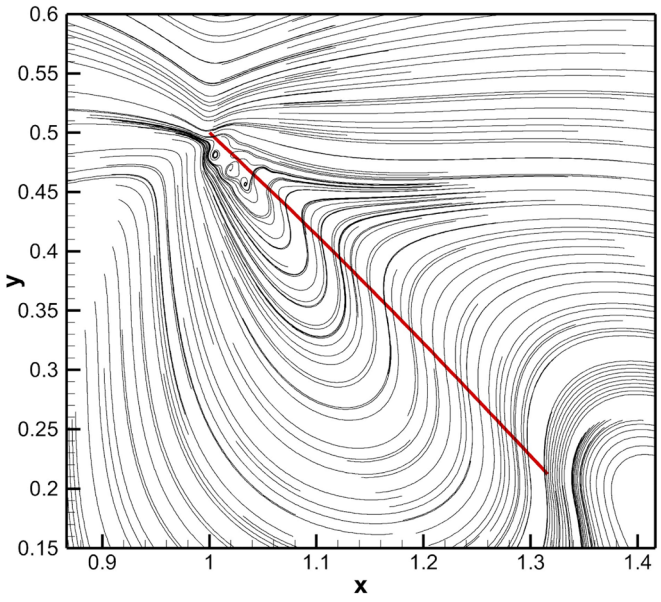

a. Filament initially placed at an angle of 45° to channel centerline at t =0.0.

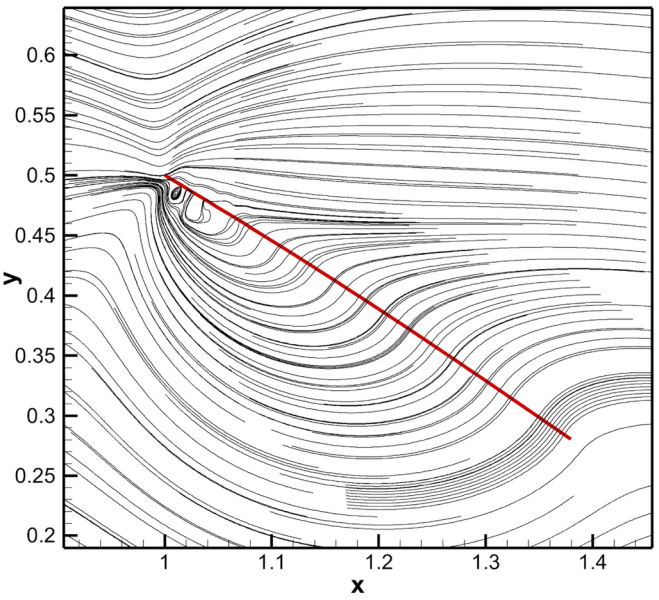

b. Filament deformation and flow field at time t = 0.15

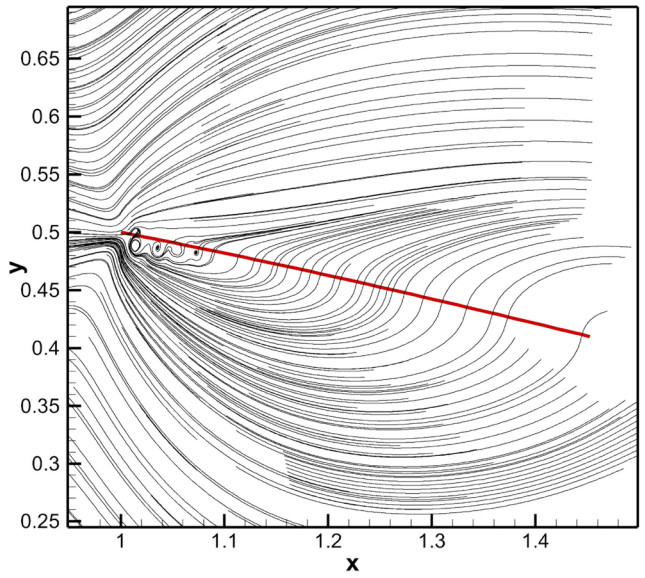

c. Filament deformation and flow field at time t = 0.30

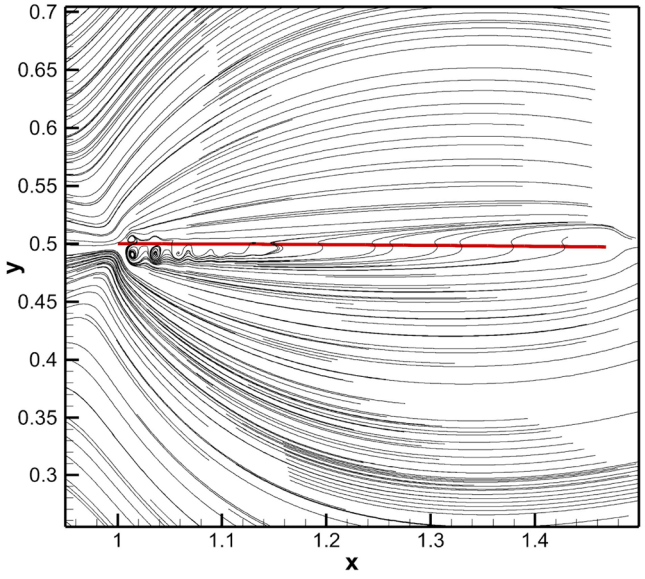

d. Filament deformation and flow field at time t = 0.60

Fig. 3. Filament deformations for different time intervals from t = 0.0 to t = 0.6.

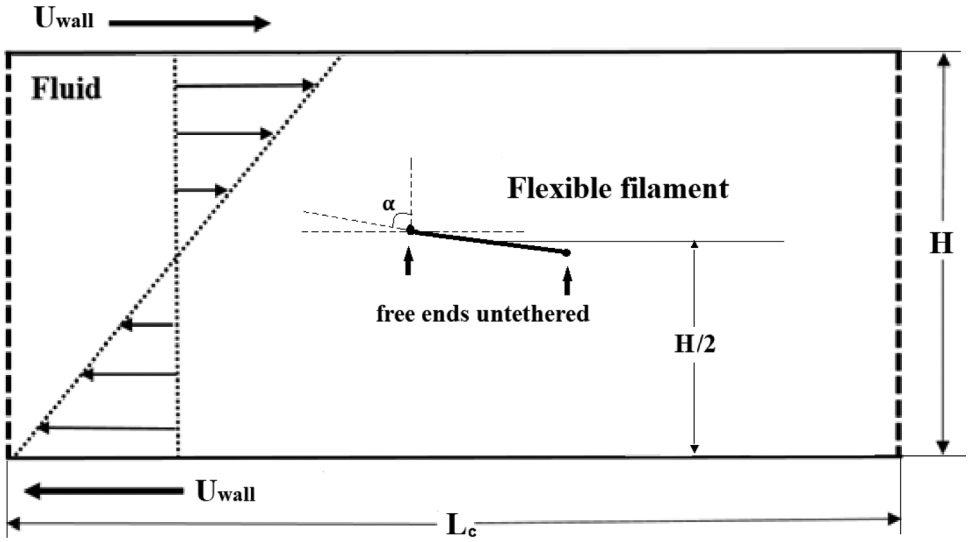

Fig. 4. Schematic illustration of flexible filament placed untethered in viscous shear flow.

$t = 0.6$, the filament attains mechanical equilibrium straight state, and no further motion or deformation is seen. A qualitative similarity is achieved in filament deformations and flow fields when compared with the results of Vahidkhah et al. (Refer to Fig. 5 and Fig. 9a in (Vahidkhah and Abdollahi, 2012)). This proves the validity of the developed model.

3.2. Filament in shear flow

The verified numerical model is modified to incorporate the physical problem of flexible filament subjected to shear flow. Forgacs et al. (Forgacs and Mason, 1959) had performed experimental studies, and Lindstrom et al. (Lindström and Uesaka, 2007), Stokie et al. (Stockie and Green, 1998) and Weins et al. (Wiens and Stockie, 2015) had carried out numerical simulation on dynamics of the flexible filament by varying filament length, shear rate and bending rigidity. They were successful in categorizing filament deformation into various orbit classes. The present two-dimensional model is employed to obtain these filament orbit classes. A schematic representation is provided in Fig. 4 which depicts a flexible filament placed freely in channel midplane subjected to viscous shear flow. In the figure, α is the angle made by the filament with respect to the vertical. The dimensional physical parameters are provided in Table 3. In order to bring an asymmetry in filament motion, the filament is initially placed at an inclination angle of 5° A large value of stretching co-efficient is assumed in-order to maintain filament inextensibility constraint. The physical parameters are non-dimensionalized with respect to characteristic length and velocity. The dimensionless filament length, shear rate, and bending rigidity are given as L, K, and K_b respectively.

The snapshots of fiber deformation for different values of filament length, shear rate, and bending stiffness is provided in Fig. 5. Rigid filament rotation is observed for high bending rigidity $K_b = 1.0$. The filament initially in an inclined position undergoes rotation and remains in the straight undeformed state throughout the rotation. When bending rigidity is reduced to 0.7, the filament undergoes slight bending at the center to form springy deformation. Further reduction in bending rigidity to 2.5×10^{-2} causes the filament to buckle about its center thereby deforming into C-shape and at $K_b = 6 \times 10^{-3}$, S-shape filament deformation is captured. With the reduction in bending rigidity, the filament can no longer resist the hydrodynamic stresses acting on its surface. Finally, complex deformations are seen for $K_b = 5 \times 10^{-4,}$ and the filament cannot retain its original straight shape.

Table 3
Physical parameters used for the filament in the shear flow simulation study.

Physical parameters	Dimensional values
Channel height (H*)	0.5 cm
Channel width (Lc*)	2.0 cm
Fluid Density (ρ)	1.0 g/cm^3
Fluid Viscosity (μ)	8 – 10 g/cm.s
Shear rate (G*)	8 – 64 /s
Filament length (Lf*)	0.1 – 0.3 cm
Bending stiffness (EI)	1.0 – 5.0 × 10–4 g.cm^3/s^2
Reynolds number (*Re*)	0.1 – 0.5

In order to further demonstrate the ability of the present model to capture filament deformation and shape formation in shear flow, angle (α) made by the filament with respect to the vertical is analyzed for two cases of filament deformation. One for the rigid case and other for S -shape deformation case. Since the filament is initially inclined at 5°, the angle (α) made by it with respect to vertical is 85° Fig. 6 compares angle (α) for two cases with respect to time. The time taken for the deformation of the flexible filament (S -shape) is faster when compared to rigid filaments as seen in Fig. 6. Also, with the completion of the first filament deformation cycle, the filament either rigid or flexible has a tendency to remain in horizontal equilibrium position for an extended period of time. This is seen in Fig. 7 which compares the angle (α) made by a filament for rigid, springy and C-shape deformation cases with respect to time. Similar observations were reported by Stokie et al. (Stockie and Green, 1998). Thus, the present model successfully demonstrates its qualitative ability to yield filament dynamics as observed in previous experimental and numerical studies with the planar shear flow.

Further, it is widely known that Jeffery's equation (Jeffery, 1922) is used to describe the motion of rigid fibers in shear flow. The Jeffery's equation is given in Eq. (26).

$$A(t) = \tan^{-1}\left(r_e \tan\left(\frac{K\, r_e t}{r_e^2 + 1}\right)\right) \tag{26}$$

where, α (t) is the angle made by the rigid filament with respect to vertical, K is the shear rate and r_e is the filament aspect ratio. A numerical simulation is carried out for fixed filament length $L = 0.3$, fixed bending rigidity EI = 1.0 and three different values of shear rate ($K = 8, 16, 32$) specifically for the case of a rigid filament. The angle (α) made by the filament with respect to the vertical for the above three

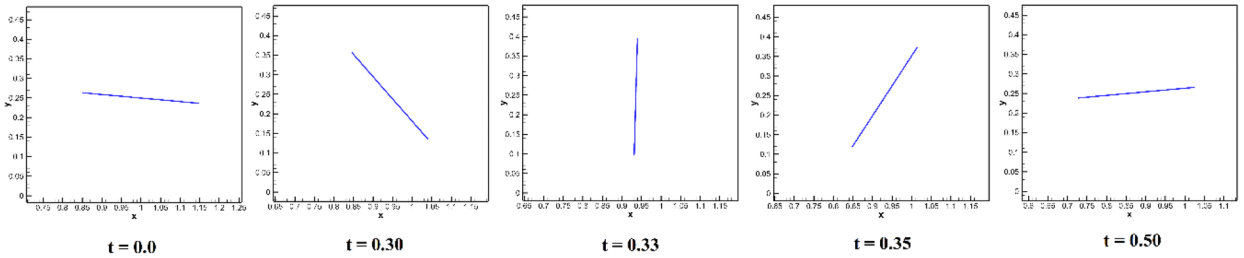

a) Rigid deformation (L = 0.3, K = 32, K_b = 1.0)

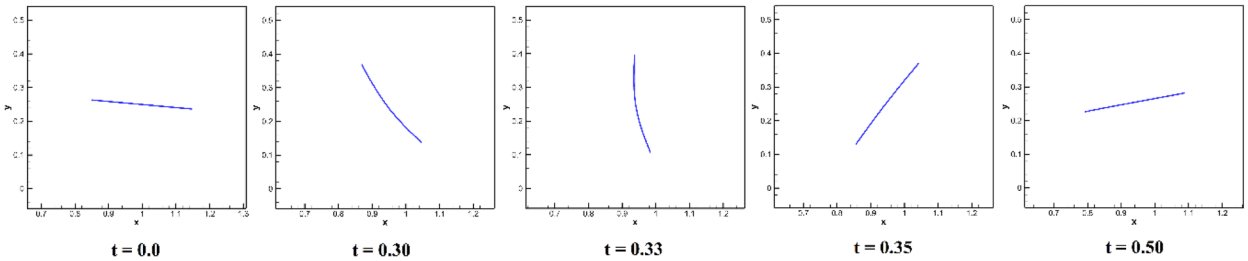

b) Springy deformation (L = 0.3, K = 32, K_b = 0.7)

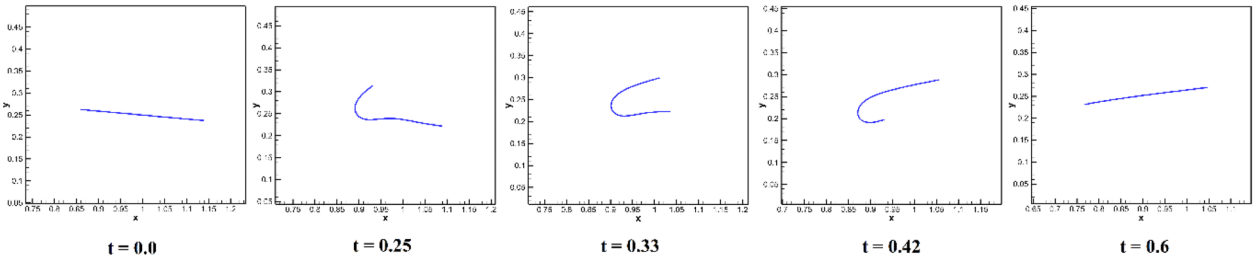

c) Snake turn (C- shape) deformation (L = 0.3, K = 32, K_b = 2.5 X 10^{-2})

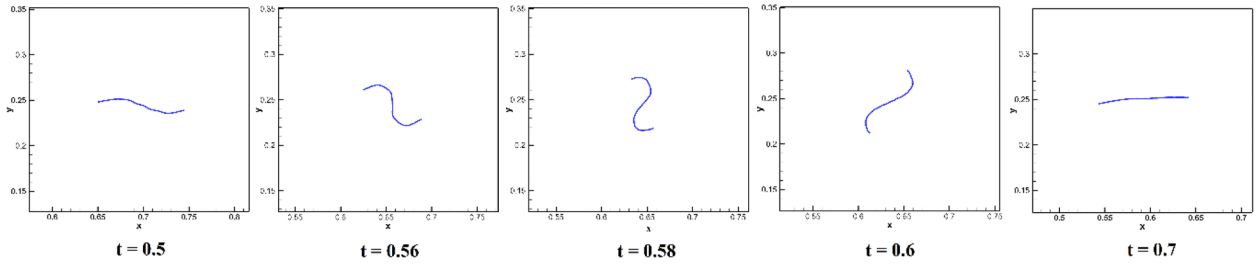

d) S – shape deformation (L = 0.1, K = 64, K_b = 6 X 10^{-3})

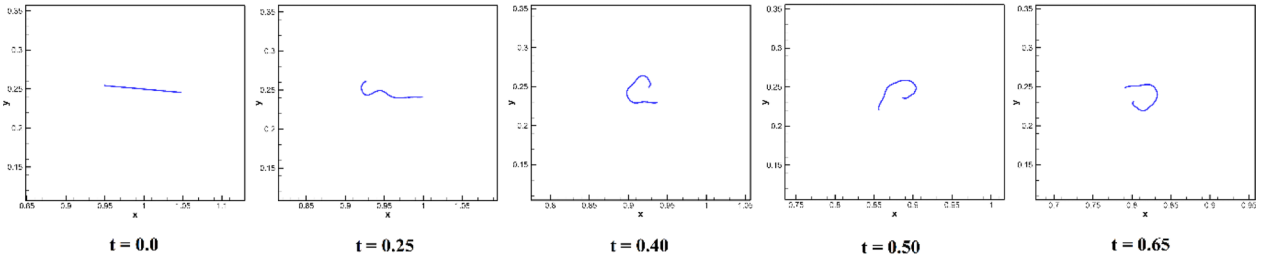

e) Complex deformation (L = 0.1, K = 64, K_b = 5 X 10^{-4})

Fig. 5. Deformation of filament at different time instances for Rigid, Springy, C-shape, S-shape and Complex orbit classes for parameters defined in Table 3.

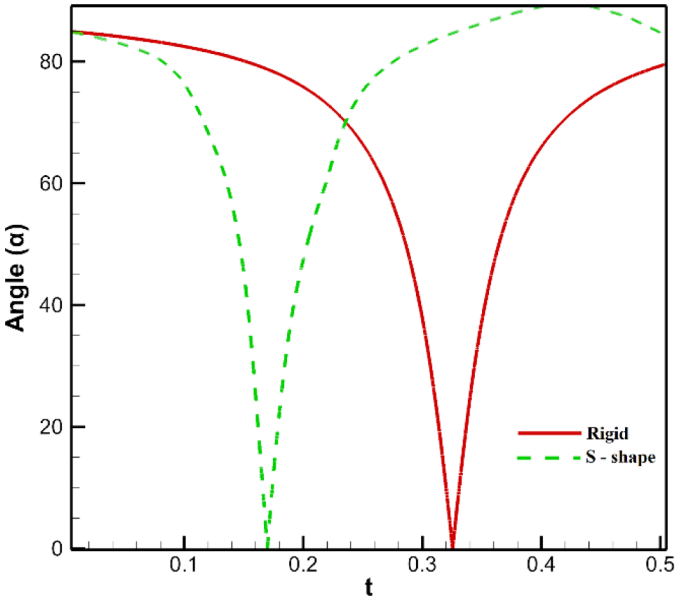

Fig. 6. Comparison of angle (α) for rigid and flexible filament (S-shape) case.

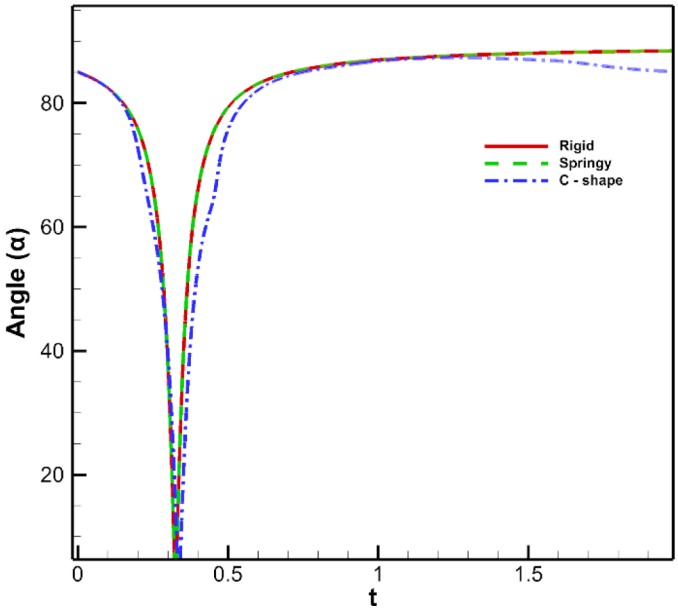

Fig. 7. Angle (α) made by the filament for different orbit classes.

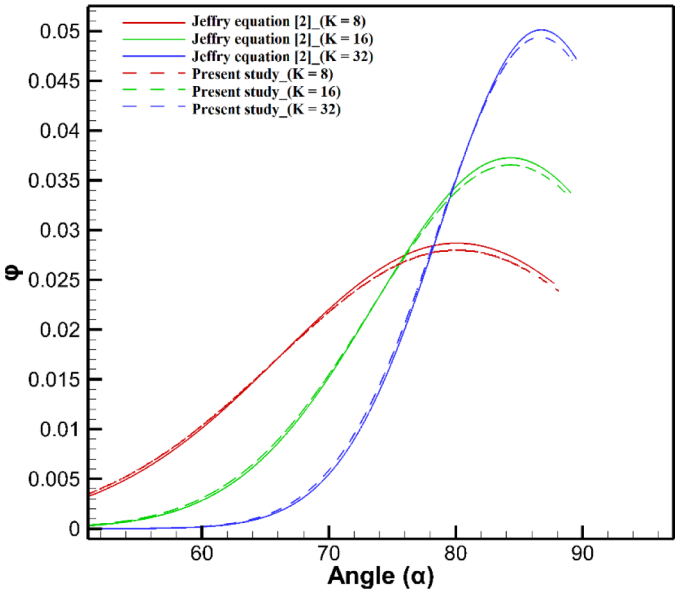

Fig. 8. A probability distribution plot indicating the time spent by the rigid filament at various angles (α).

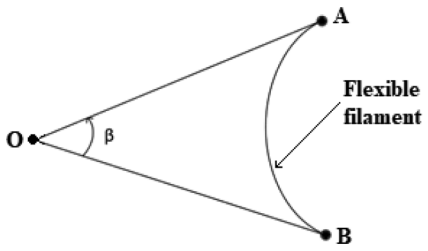

Fig. 9. Exterior angle β, defined between the ends A and B of the filament.

test cases is recorded. The total simulation time is maintained at $t = 3.0$. The angle α (t) based on Jeffery's equation is also determined for the above same set of shear rates by fixing the aspect ratio $r_e = 60$. Cylindrical fibers of length 0.1 to 0.3 typically have aspect ratio r_e ranging between $60 \leq r_e \leq 400$ (Stockie and Green, 1998). Similar to Stokie et al. (Stockie and Green, 1998), a probability distribution φ indicating the time spent by the filament at various angles (α) is plotted in Fig. 8 for both the present simulation results and Jeffery's equation results. As seen from the plot, our results are found to be in good agreement with Jeffery's equation.

Finally, a detailed parametric analysis is performed for fixed filament length $L = 0.1$, three different values of shear rates ($K = 10$, 16, 32) and 14 different values of bending rigidity (EI). The Viscous Flow Forcing value (VFF) is also calculated. For each of the 42 parametric test conditions, an additional parameter called exterior angle β defined as shown in Fig. 9 is determined. In the figure, A and B are the ends of the filament and connected to a fixed-point O (Refer to Fig. 11 in (Stockie and Green, 1998)). Stokie et al. (Stockie and Green, 1998) had developed a criterion based on the exterior angle (β) to classify filament orbit classes. The filament can be considered to be rigid if $175^\circ < \beta < 180^\circ$, the filament is springy if $90^\circ < \beta < 175^\circ$ and for $\beta < 90^\circ < 30^\circ$, the filament ends move independently of each other forming C-shapes. Further, from the filament deformations, it is observed that complex shape orbit class can be specified for $\beta < 30^\circ$ The resulting flexible filament regimes are classified and plotted in Fig. 10 with respect to Viscous Flow Forcing value (VFF) and bending rigidity (EI). Along with the present simulation results, the experimental results of Forgacs et al. (Forgacs and Mason, 1959) and numerical results of Stokie et al. (Stockie and Green, 1998) are also included in the classification plot.

In Fig. 10, the vertical solid lines demarcate filament orbit regimes. In the plot, the black solid points indicate experimental results of Forgacs et al. (Forgacs and Mason, 1959), the colored open points indicate numerical results of Stokie et al. (Stockie and Green, 1998) and colored solid points indicate present simulation results. As observed from Fig. 10, most of the present study results coincide with experimental results of Forgacs et al. (Forgacs and Mason, 1959) and numerical results of Stokie et al. (Stockie and Green, 1998), especially for rigid, springy and C-shape regimes. The division in orbit regimes from rigid to springy to C-shape are obtained at VFF = 0.16, 1.31 and 10.67, consistent with the criterion stipulated by Stokie et al. (Stockie and Green, 1998). Thus, the results of the present study are found to be in excellent agreement with previous experimental and computational results. The two aspects discussed in Fig. 8 and Fig. 10 serve as the

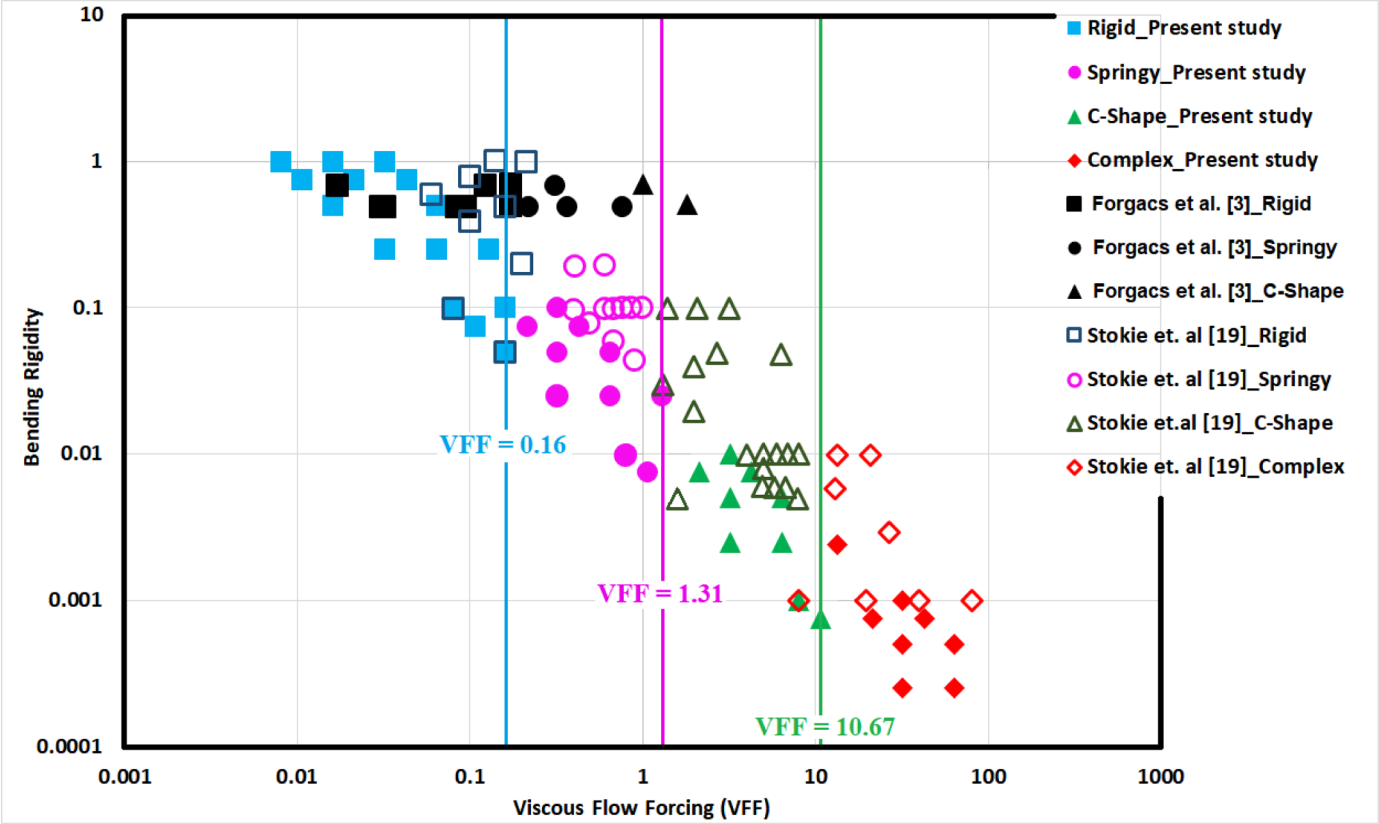

Fig. 10. Classification of flexible filament deformation into various orbit classes like Rigid, Springy, C – Shape and Complex shapes.

Table 4
Physical parameters and dimensionless values considered for the two-dimensional simulation of diatom chain.

Physical Parameters	Dimensional value	Non-dimensional value
Filament length (L_f^*)	0.47mm	0.25
	0.58mm	0.3125
Shear rate (G^*)	0.5/s	1.0
	1.0/s	2.0
Bending rigidity (EI)	5.72×10^{-16} Nm^2	1×10^{-4}
	5.72×10^{-17} Nm^2	1×10^{-5}

quantitative validation for the present model. All of the above results and observations actively demonstrate the ability of our developed model to simulate the dynamics of a flexible filament in shear flow.

Next, the two-dimensional simulation of diatom chains in viscous shear flow is considered. The case analyzed here is that of unicellular phytoplankton which is a non-motile diatom made up of linkages. The diatom chains are thus modeled in the present study as flexible filaments. The phytoplankton (diatom chains) in the ocean typically experience shear rate in the range of 0.01 to 1 s^{-1}. Also, the length of the diatom chains is estimated to be between 0.25 mm to 4 mm. The limits for both shear rate and characteristic length observed for diatom chains is ascertained by Karp–Boss et al. (Karp-Boss et al., 1996). The Reynolds number which depends on shear rate and diatom chain length for this case lies between $6.25 \times 10^{-4} \leq Re \leq 16$ as confirmed by simulation studies of Nguyen et al. (Nguyen and Fauci, 2014). Considering the properties of seawater and bending rigidity of diatom chains, the Reynolds number for the present study is fixed at 1.75. Here, the Reynolds number is computed based on the length of the filament as characteristic length and oceanic shear rate as the reference for characteristic velocity. The chosen physical parameters and their corresponding non-dimensionalized values are tabulated in Table 4.

In order to perform the parametric study, eight different cases are analyzed based on non-dimensionalized filament length (L), shear rate (K) and bending rigidity (K_b). In order to simplify explanations for various cases, the filament having length $L \leq 0.25$ are considered short and that with length $L > 0.25$ are considered as long. Also, filaments with bending rigidity $K_b = 1 \times 10^{-4}$ are identified as type-A, and those with rigidity $K_b = 1 \times 10^{-5}$ are called type-B. The chosen bending rigidity of diatoms lies between that of L. annulata and G. delicatula species. The shear rate and Reynolds number in our study are very similar to that experienced by diatom chains in the ocean.

The continuity and momentum equations are solved on a two-dimensional rectangular channel of dimensionless length 8.0 and height 1.0. The fluid domain is made up of 1024×128 grid points and a time step of 1×10^{-5} is used to satisfy the stability of the numerical scheme. The physical problem defined for this study consists of a flexible filament held horizontally at the center position of the simulation domain. The filament is modeled with 100 IB points. In literature, it is observed that the flexible filament is initially curved and placed horizontally at the channel midplane. This will help the filament to come out of the mechanical equilibrium position and subsequently undergo deformations. However, in the present study, the filament is kept inclined at a particular angle to the horizontal in order to allow it to deviate from its equilibrium position. When diatom chain simulation is performed, the filament would initially take considerable amount of time to undergo any significant deformation. Thus, it is necessary to maintain a higher initial angle of inclination of 10° so as to obtain different filament orbits in a reasonable amount of time. The filament is placed at the center of the computational domain at location (4, 0.5). The value of stretching co-efficient K_s is fixed as 5000 for all cases. A computer code based on FORTRAN is developed to perform two-dimensional simulations. The simulations are carried out for $t = 60.0$, and the evolution of diatom links for each case is systematically investigated. The deformation of the filaments is recorded at respective time intervals for all cases.

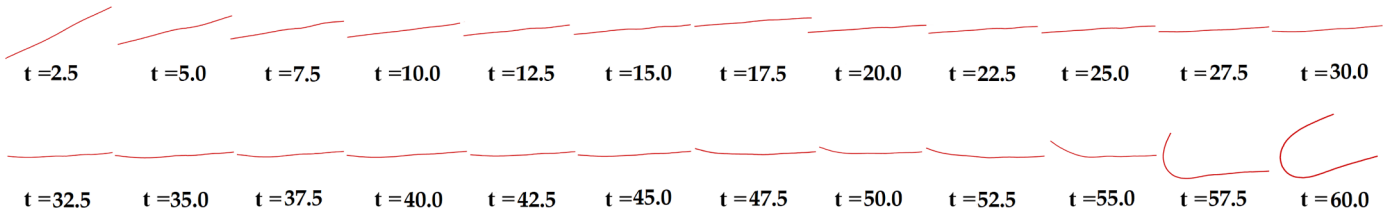

Fig. 11. Evolution of filament subjected to shear flow for $L = 0.25$, $K = 1.0$, $K_b = 1 \times 10^{-4}$.

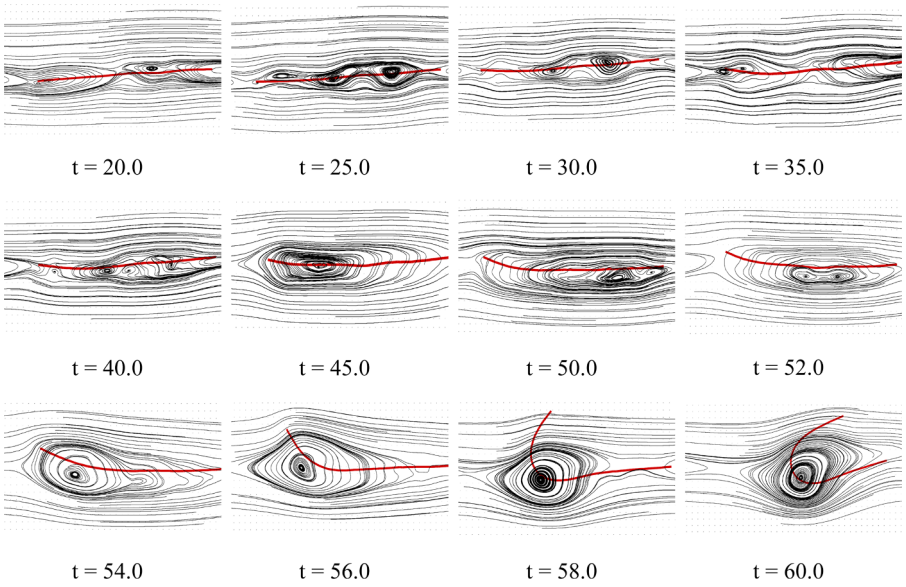

Fig. 12. Streamlines obtained at the vicinity of filaments at different time sequences for $L = 0.25$, $K = 1.0$, $K_b = 1 \times 10^{-4}$.

3.3. Case study

The evolution of filament collectively depicts the various deformation states the filament undergoes at different time steps. The study is carried out by performing simulations for short and long filaments based on their lengths. Also, shear rates and bending rigidity are varied.

Case 1: $L = 0.25$, $K = 1.0$, $K_b = 1 \times 10^{-4}$.

The filament belonging to this group is short, type-A and subjected to a lower shear rate. Figs. 11 and 12 show filament evolution and streamlines obtained near the filament surface respectively. In Fig. 11, the filament does not deform for the initial time sequence and remains in the horizontal position for a larger portion of simulation. At $t = 54.0$ (Fig. 12), the filament breaks symmetry and at $t = 60.0$ folds onto itself to form a C-shape buckling. Similar shapes were reported in the experimental works of Forgacs et al. (Forgacs and Mason, 1959), numerical studies of Stokie et al. (Stockie and Green, 1998; Stockie, 2002) and Ross et al. (Ross and Klingenberg, 1997). These deformations are referred to as snake turns. No form of shape replication is observed. A sequence of single and multiple recirculation zones are observed throughout. Streamlines as observed at $t = 50.0$ (Fig. 12), show the formation of a large elliptical recirculation zone at the bottom right portion of the filament. This zone travels left along the filament surface. At $t = 54.0$, the zone grows sufficiently large to push the filament upwards thus making the filament to bend at the center. The formation of such large primary circulation zones indicates symmetry breakage for filaments.

Case 2: $L = 0.25$, $K = 2.0$, $K_b = 1 \times 10^{-4}$.

The filament in this group is short, type-A and subjected to higher shear rate. Figs. 13 and 14 show filament evolution and streamlines obtained near the filament surface respectively. Symmetry breaks at $t = 22.0$ as seen in Fig. 14. The filament undergoes a snake-like turn and returns back to a horizontal, inclined position at $t = 30.0$. The deformation time t_d is observed to be 4.0 (between $t = 22.0$ and $t = 26.0$). When filament deformation is observed at $t = 25.0$ and at $t = 47.5$, a snake turn shape replication is seen (Fig. 13). The images at $t = 14.0$,16.0, 18.0 and 20.0 (Fig. 14) show multiple recirculation zones along the length of filament owing to instability caused by the combination of fluid impingement and compression states of the filament . Similar to Case 1, a large elliptical zone is produced at left filament corner which pushes it upwards. At $t = 30.0$ (Fig. 14), the elliptical zone spans across the entire length of the filament with the recirculation center close to filament midpoint.

Case 3: $L = 0.25$, $K = 1.0$, $K_b = 1 \times 10^{-5}$.

The filament is type-B, short and subjected to a lower shear rate in this case. Figs. 15 and 16 show filament evolution and streamlines obtained near the filament surface respectively. The symmetry break occurs early at $t = 24.0$ (Fig. 16), thus highlighting that symmetry break occurs faster for type-B filaments when compared to type-A as in case 1. When the filament is observed at $t = 32.5$ (Fig. 15), an incomplete “S” shape is seen. Such S-turns are a characteristic feature of flexible filaments, and similar shapes are observed in the numerical works of Weins et al. (Wiens and Stockie, 2015), Ross et al. (Ross and Klingenberg, 1997) and experimental works of Forgacs et al. (Forgacs and Mason, 1959) . Deformation time t_d is found to be 10.0 (between $t = 24.0$ and $t = 34.0$). Also, shape replication is seen when deformation is observed at $t = 27.5$ and $t = 52.5$. In Fig. 16 at $t = 26.0$, two recirculation zones appear with the primary zone at right side and secondary zone at the left end of the filament. The primary zone pushes

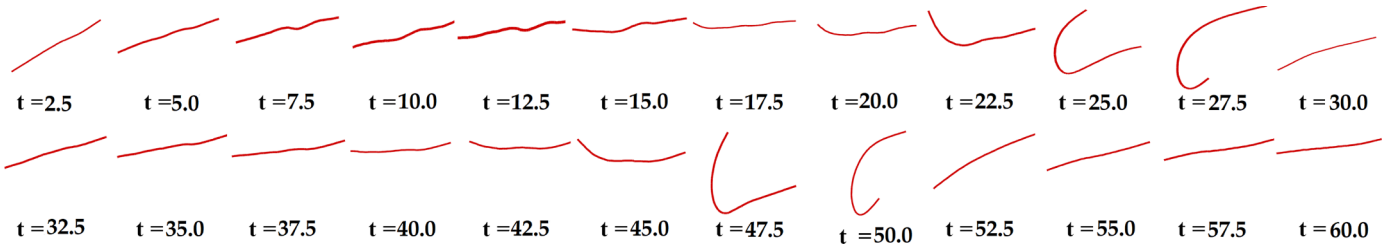

Fig. 13. Evolution of filament subjected to shear flow for $L = 0.25$, $K = 2.0$, $K_b = 1 \times 10^{-4}$.

the right side of the filament downwards whereas the secondary zone pushes the left tip upwards. This can be observed at $t = 28.0$ in Fig. 16. As time advances, the secondary zone is absorbed by the primary one to form a single eye shaped recirculation zone at $t = 32.0$. The center of the primary zone splits up and then merges back to form a circularly shaped zone at $t = 36.0$. Finally, the filament reaches the horizontal position with an elliptical zone spanning the entire filament length at $t = 42.0$. The replication of S-shape begins at $t = 44.0$. Primary and secondary zones are observed at $t = 48.0$. However, the secondary zone is unable to grow to a bigger size as seen at $t = 28.0$ which prevents the left filament tip to move upwards, and thus the left portion aligns with the primary zone. This leads to the formation of C-shape buckling, and hence a combination of S and C-shapes are observed throughout in Fig. 16. Throughout the simulation, the ends of the filament never return back to its original position and remain in a deformed state, thus indicating non-recuperation.

Case 4: $L = 0.25$, $K = 2.0$, $K_b = 1 \times 10^{-5}$.

In this case, the filament is type-B, short and subjected to higher shear rate. Figs. 17 and 18 show the evolution pattern and corresponding streamlines obtained near the filament surface. Symmetry breaks early at $t = 7.5$ (Fig. 17). The lowest end-to-end distance d_{ee} is seen at $t = 15.0$. Deformation time t_d is found to be 7.5 (between $t = 7.5$ and $t = 15.0$). Folding of the filaments occur at $t = 15.0$, $t = 25.0$ and close to $t = 32.5$. Beyond this point, a transition of filament shape from straight to S-shape occurs between $t = 40.0$ to $t = 48.0$. The mechanism with which S-shape is formed is similar to Case 3. However, an important aspect of this case is the formation of two equally sized recirculation zones post S-shape formation. This is observed at $t = 50.0$.

Case 5: $L = 0.3125$, $K = 1.0$, $K_b = 1 \times 10^{-4}$.

Fig. 19 depicts a type-A, long filament subjected to lower shear rate. Fig. 20 shows the streamlines obtained near the filament surface. Symmetry break occurs at $t = 58.0$ (Fig. 20), which is closer to the simulation end time. No substantial deformation is observed making it similar to Case 1. This also indicates that longer filaments tend to take more time compared to short filaments to undergo noticeable deformation when subjected to the same shear flow conditions. The formation mechanism of C-shape buckling is similar to Case 1. Throughout the simulation, multiple recirculation zones ranging from two to four are observed near the filament surface.

Case 6: $L = 0.3125$, $K = 2.0$, $K_b = 1 \times 10^{-4}$.

In this group a type-A, long filament subjected to higher shear rate is considered. Figs. 21 and 22 depict filament evolution and resulting streamlines near the surface respectively. The filament remains horizontal for the first half of the total simulation time and undergoes symmetry break at $t = 30.0$. Snake-like turns are also observed here which is similar to case 2. The deformation time t_d is observed to be 4.0 (between $t = 30.0$ and $t = 34.0$). Replication of the snake turn shape occurs when observed for deformation at $t = 34.0$ (Fig. 22) and $t = 57.5$(Fig. 21). The ends of the filament return back to its original position, thus showing rigidity. The mechanism of snake turn is similar to Case 2.

Case 7: $L = 0.3125$, $K = 1.0$, $K_b = 1 \times 10^{-5}$.

Fig. 23 illustrates the deformation of type-B, long filaments in the fluid flow of high shear rate. Fig. 24 show streamlines occurring near

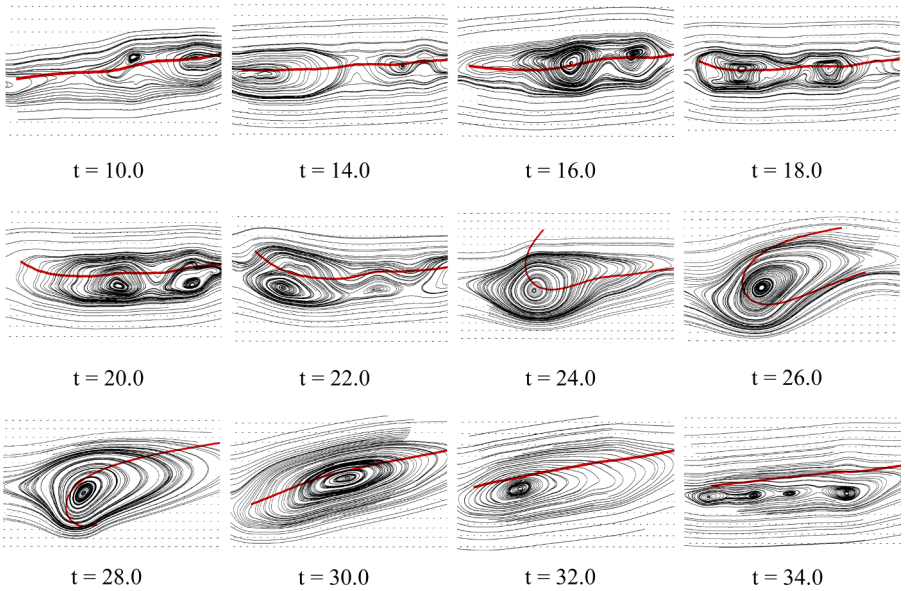

Fig. 14. Streamlines obtained at the vicinity of filaments at different time sequences for $L = 0.25$, $K = 2.0$, $K_b = 1 \times 10^{-4}$.

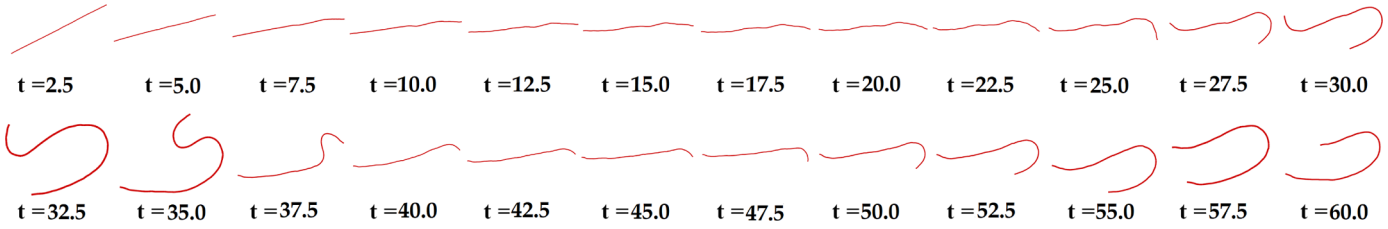

Fig. 15. Evolution of filament subjected to shear flow for $L = 0.25$, $K = 1.0$, $K_b = 1 \times 10^{-5}$.

the surface of the filament. The deformations observed are very similar to Case 3. The symmetry breaks at $t = 27.5$. An incomplete S-shape is formed at $t = 37.5$. The mechanism of S shape formation is very similar to Case 3 given in Fig. 16. Shape replication is observed for $t = 35.0$ and $t = 57.5$. It can be seen in Fig. 16 corresponding to Case 3 that the filament gains S-shape. However, when observing the same filament from $t = 50.0$ to $t = 60.0$, there is a transition to C-shape. Such transitions are not observed here, and S-shapes appear to occur in a cyclic manner. This may be due to the extended length of the filament in the present case. The streamlines from $t = 50.0$ to $t = 60.0$ are shown in Fig. 24.

Case 8: $L = 0.3125$, $K = 2.0$, $K_b = 1 \times 10^{-5}$.

In the last case, the filament considered is type-B, long and subjected to a high shear rate. The symmetry break is obtained at $t = 10.0$ as seen in Fig. 25. Fig. 26 shows the streamlines obtained near the filament surface for complex shapes. A wide range of complete and incomplete S-shapes are observed during the simulation. The filament undergoes incomplete S turns at $t = 17.5$ and $t = 35.0$, while complete S-turns are found at $t = 42.5$ (Fig. 25) and $t = 50.0$ (Fig. 26). Shape replications are obtained for $t = 30.0$ and $t = 60.0$. The deformation time t_d is observed to be 7.5 (between $t = 10.0$ and $t = 17.5$).The filament is highly flexible in nature and produces the highest number of turning point replications. It shows the least resistance to fluid flow. Along with S-turns, some complex shapes have also been found at $t = 27.5$, 37.5 and 52.5 (Fig. 25). Apart from $t = 38.0$ and $t = 42.0$, all images show one large circular recirculation zone around which the filament rotates.

The dimensional physical parameters available in Table 4 are required for the calculation of Viscous Flow Forcing value (VFF) for all the cases considered. The same is calculated and provided in Table 5.

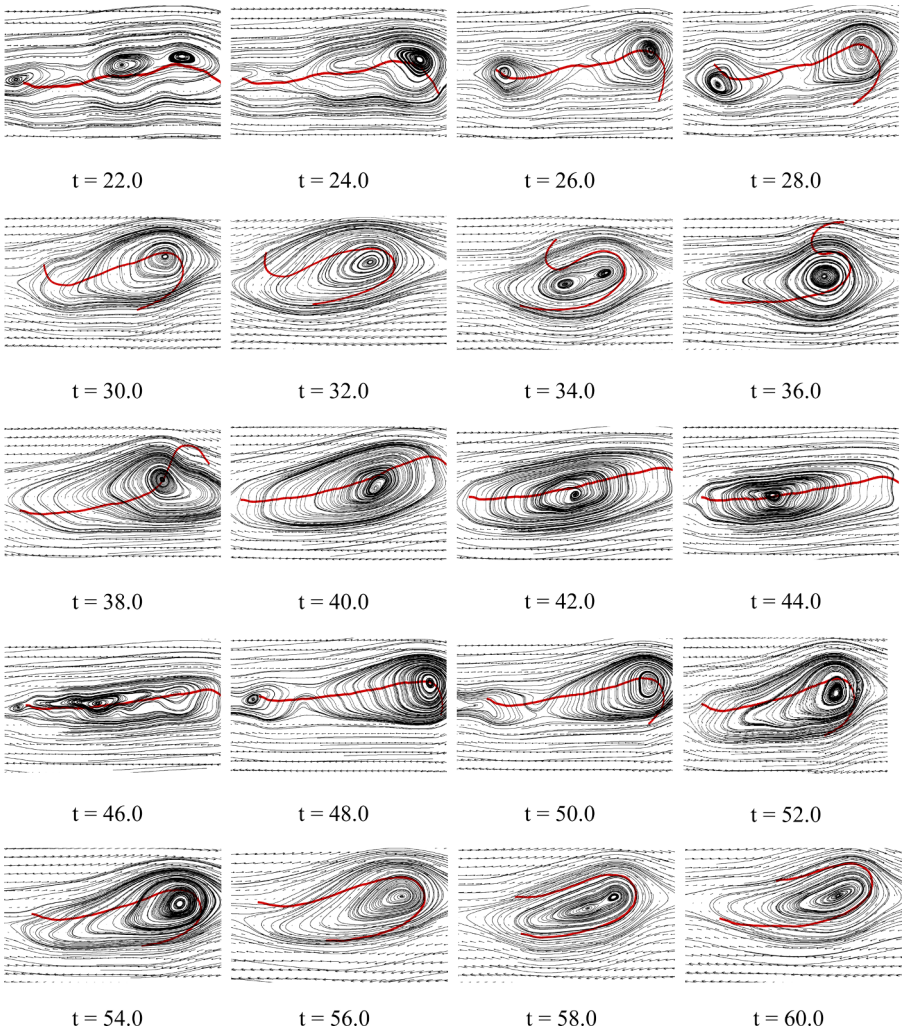

Fig. 16. Streamlines obtained at the vicinity of filaments at different time sequences for $L = 0.25$, $K = 1.0$, $K_b = 1 \times 10^{-5}$.

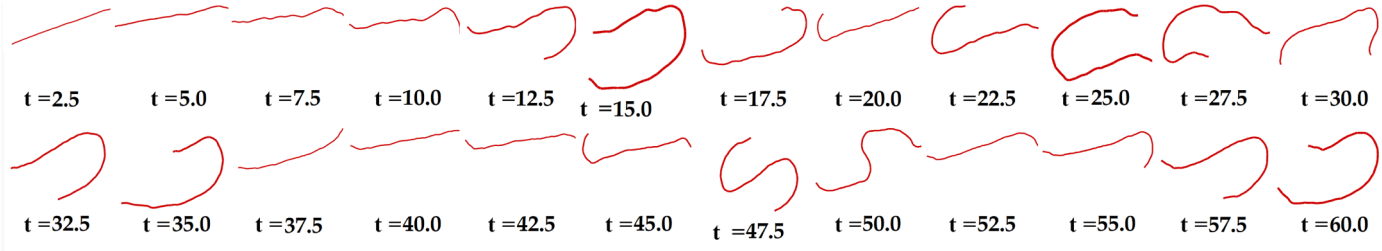

Fig. 17. Evolution of filament subjected to shear flow for $L = 0.25$, $K = 2.0$, $K_b = 1 \times 10^{-5}$.

The Viscous Flow Forcing value for the present diatom chain problem involving all the test cases ranges from $5.0 \times 10^{-4} \leq$ VFF $\leq 1.1 \times 10^{5}$ as provided in the simulation studies of Nguyen et al. (Nguyen and Fauci, 2014). By observing the Viscous Flow Forcing term calculated for all cases in Table 5 and by analyzing filament deformation from the case study, it is ascertained that Cases 1,2,5 and 6 all produce VFF value less than 350. These are also the cases for which the filaments undergo initial deformation and with the progression of simulation time retain their original shape. Filaments belonging to these groups are thus classified as recuperative. Recently, Liu et al. (Liu et al., 2018) analyzed the morphological transitions of elastic filaments in shear flow. The transition between different orbit classes or regimes of elastic filaments is studied using experimental and local slender-body theory. Tumbling, C-buckling and U-turn regimes are observed and their corresponding Viscous Flow Forcing values are calculated. In their theoretical study, the filament contour lengths are in the range 4 - 40 μm and shear rate is in the range 1–10 s^{-1}. In the experimental setup, the Reynolds number is of the order 10^{-4}. For the case of non-Brownian filament motion, the first transition from tumbling to C-buckling occurs at a Viscous Flow Forcing value of 306.4 which is also verified by them through experiments. A phase chart diagram (Refer to Fig. 4 in (Liu et al., 2018)) is also provided by them to highlight the various filament transition regimes. The filament is highly recuperative in nature and beyond the Viscous Flow Forcing value of 306.4, the filament transitions from C-buckling to U-turn shape indicating non-recuperative behavior. Accordingly, our results are in reasonable agreement with that of Liu et al. (Liu et al., 2018).

Filaments belonging to Cases 3,4,5 and 7 have VFF value higher than 350. These filaments never retain their original shape once initially deformed. Thus they can be grouped as non-recuperative. The fluid motion or pattern of recirculation zones leading to the formation of snake turns (C-shape) and S-shapes are similar in all cases. Fluid flow around recuperative filaments as observed in Case 1 and Case 5 show the formation of single and multiple recirculation zones along the length of the filament. This is an indication of filament resistance to fluid motion. The flow is drag induced making it an ideal condition for nutrient absorption in diatoms (Karp-Boss et al., 1996). Also, recuperative filaments produce flat elliptical zones around the filament body as compared to non-recuperative ones which produce circularly shaped zones. Elliptical zones prevent nutrients from spreading locally, thus providing diatom with a rich nutrient surrounding. Long recuperative filaments deform at a slow pace when compared to short filaments. An increase in length also contributes to more number of zones. Short filaments as in Cases 3 and 4 have an ability to transit from S-shape to C-shape irrespective of their bending rigidity. However long filaments have cyclic nature of shape formation without transitions. The non-reuperative filaments tend to deform faster along the orbit of the circulation zone and also show less resistance to fluid motion. This prevents the filament from sweeping nutrients as compared to recuperative filaments (Case 2 and Case 6).

In the above case study, the analysis was carried out for a fixed Reynolds number $Re = 1.75$. Now let us examine the effect of varying Reynolds number on diatom chain deformations. Two Reynolds numbers ($Re = 0.875$, by varying shear rate) and ($Re = 8.0$, by varying diatom chain length) are computed. The critical Viscous Flow Forcing value also varies for different Reynolds numbers. The simulations for the Reynolds numbers mentioned above are carried out. The dynamics and evolution of diatom chains for these two cases of Reynolds number $Re = 0.875$ and $Re = 8.0$ is analyzed and provided in figures below.

The analysis from diatom simulation studies has revealed that up to a critical VFF value of 350, the diatom behaves recuperatively and beyond the critical value, they tend to be non-recuperative. Reducing the Reynolds number to 0.875, also causes VFF to decrease and in this case, it is 44.0. When comparing Fig. 11 pertaining to Case 1 of the present study for which $Re = 1.75$ and VFF = 89.4 and Fig. 27, we see that not much difference can be seen in filament dynamics throughout the entire simulation period, except towards the end ($t = 60.0$) where the diatom in Fig. 27 just begins to undergo buckling. Also, in Fig. 27 it can be observed that the diatom still behaves recuperatively. Thus, reducing the Reynolds number causes the diatom to deform slowly.

If the VFF value is greater than 350, the diatoms do not retain their original shape and their dynamics is concentrated more towards the formation of S-shape deformations. When observing filament evolution for higher Reynolds number, $Re = 8.0$ and VFF = 872.0 as shown in

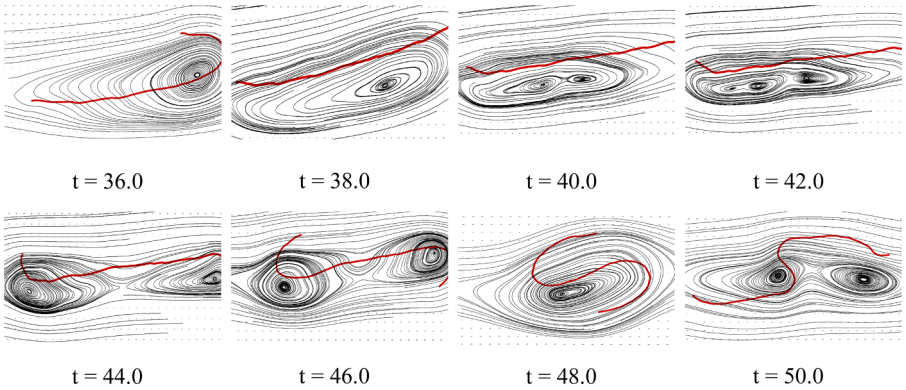

Fig. 18. Streamlines obtained at the vicinity of filaments at different time sequences for $L = 0.25$, $K = 2.0$, $K_b = 1 \times 10^{-5}$.

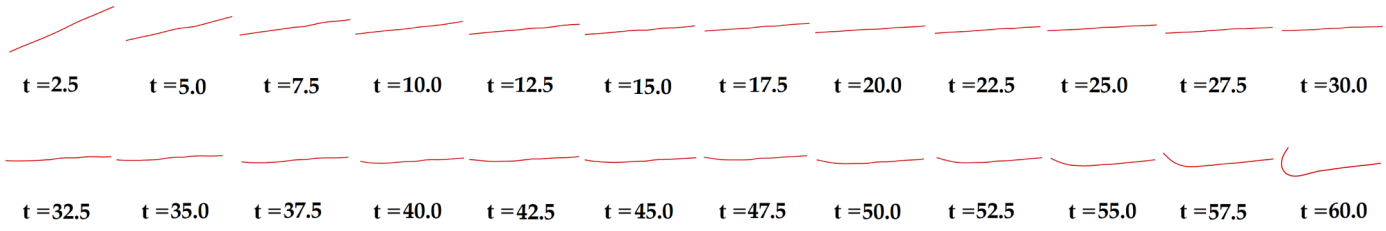

Fig. 19. Evolution of filament subjected to shear flow for $L = 0.3125$, $K = 1.0$, $K_b = 1 \times 10^{-4}$.

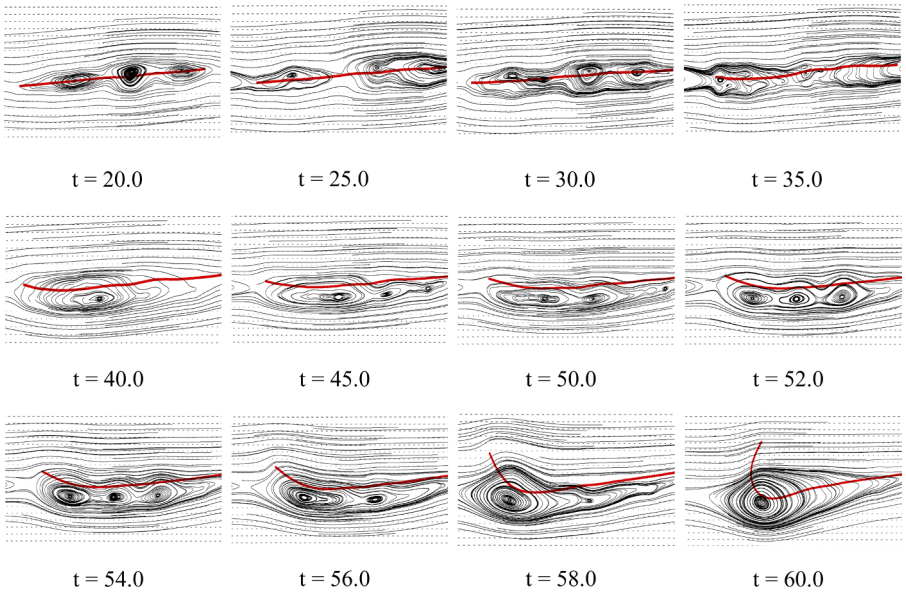

Fig. 20. Streamlines obtained at the vicinity of filaments at different time sequences for $L = 0.3125$, $K = 1.0$, $K_b = 1 \times 10^{-4}$.

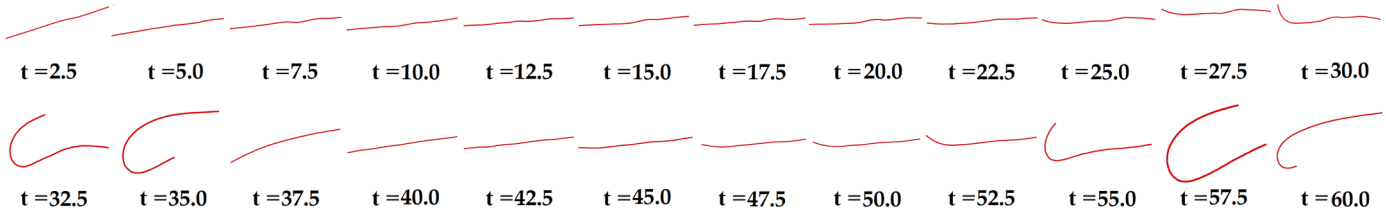

Fig. 21. Evolution of filament subjected to shear flow for $L = 0.3125$, $K = 2.0$, $K_b = 1 \times 10^{-4}$.

Fig. 28 and comparing it with Fig. 15 which belongs to case 3 of the present study for which the $Re = 1.75$ and VFF = 894.2, we see a slight deviation in filament dynamics. We also see that in Fig. 15, S – shape diatom deformation initiates and completes between time $t = 30.0$ and $t = 40.0$. A similar observation is obtained in Fig. 28 where this time gap is between $t = 30.0$ to $t = 45.0$. The slight difference may be due to variation in VFF values for both these scenarios. Higher Reynolds number produced larger Viscous Flow Forcing value. The above analysis also confirms that lower VFF value produces slower filament deformations. Even though Reynolds number is important, VFF values play a critical role in better understanding the dynamics when filaments are subjected to shear flow. Our analysis is comprehensive in that it covers VFF values for a wide range between $0 \leq \text{VFF} \leq 3500$, which includes most of the critical parameters like diatom chain length, shear rates and Reynolds numbers.

Next, we shall define some analysis factors that describe motion, shape replication and deformation of filament for the simulation cycle.

Symmetry breakage time (t_{sb}) defined as the time for which the filament breaks symmetry for the first time.
End-to-end distance (d_{ee}) defined as the distance between the two ends of the filament.
Turning point time (t_p) defined as the time at which the filament attains the lowest end-to-end distance.
Deformation time (t_d) defined as the time difference between first symmetry breakage and lowest end-to-end distance.
Recurrence time (t_r) defined as the average time difference between two successive turning point occurrences in the simulation cycle.

We now compare their effects and understand the variation for different cases. It is essential to understand the significance of symmetry breakage time t_{sb}, turning point time t_p, deformation time t_d and recurrence time t_r in the present study. Higher symmetry breakage time signifies that the filament remains in the undeformed state for a large portion of time. This gives ample time for the filament to interact with the surrounding environment. In the case of diatom chains, it provides more time for it to absorb necessary nutrients. Ideally, the diatom has to remain in the undeformed state with an assumption that the surrounding is risk-free. Remaining in the undeformed state allows orientation of filament to high drag inducing fluid motion (Guasto et al., 2012). Once deformation is initiated by fluid motion, the diatoms

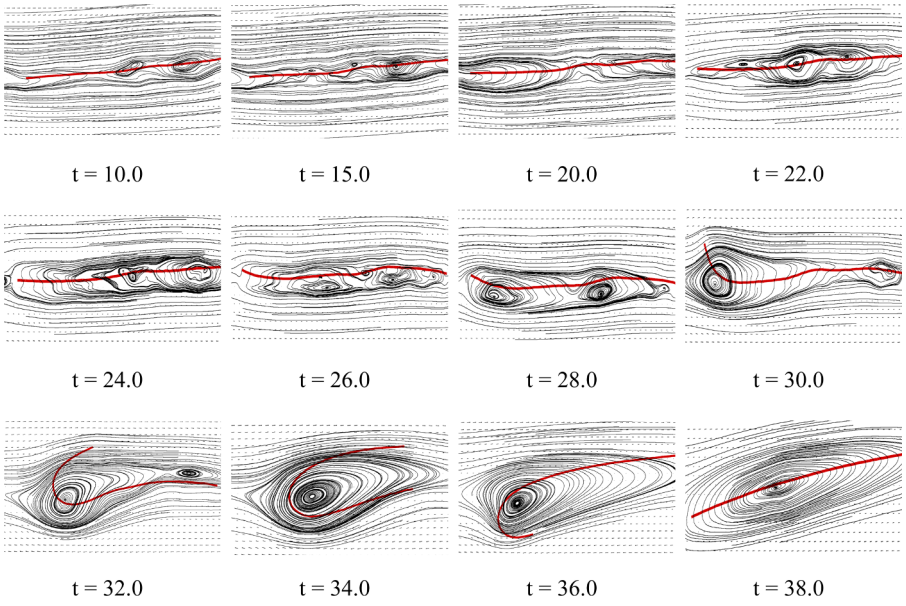

Fig. 22. Streamlines obtained at the vicinity of filaments at different time sequences for $L = 0.3125$, $K = 2.0$, $K_b = 1 \times 10^{-4}$.

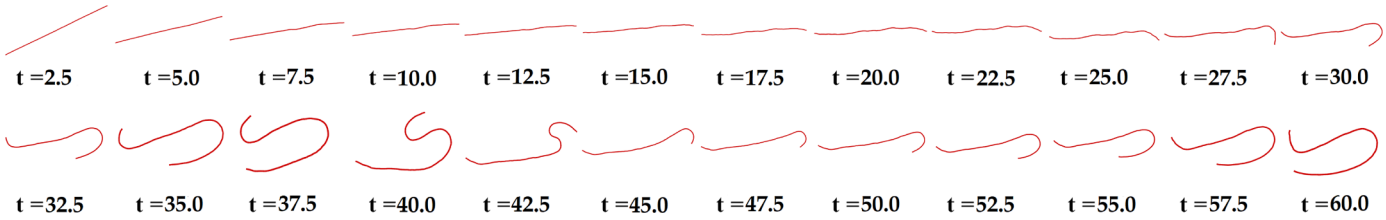

Fig. 23. Evolution of filament subjected to shear flow for $L = 0.3125$, $K = 1.0$, $K_b = 1 \times 10^{-5}$.

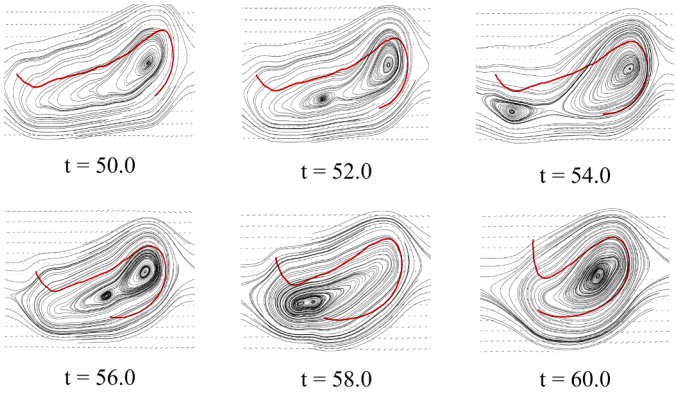

Fig. 24. Streamlines obtained at the vicinity of filaments at different time sequences for $L = 0.3125$, $K = 1.0$, $K_b = 1 \times 10^{-5}$.

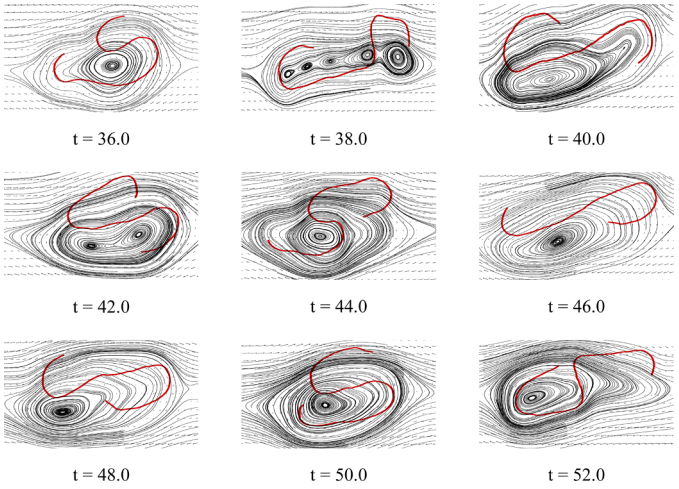

Fig. 26. Streamlines obtained at the vicinity of filaments at different time sequences for $L = 0.3125$, $K = 2.0$, $K_b = 1 \times 10^{-5}$.

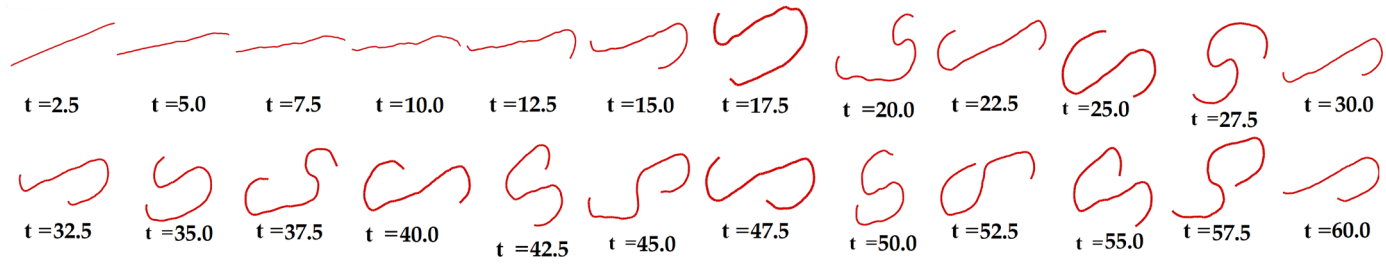

Fig. 25. Evolution of filament subjected to shear flow for $L = 0.3125$, $K = 2.0$, $K_b = 1 \times 10^{-5}$.

Table 5
Viscous Flow Forcing term (VFF) calculated for different cases of varying filament length, shear rate and bending rigidity for Reynolds number 1.75.

Case No. and condition (length, shear, rigidity type)	Diatom chain length, L_{diatom} (m) x 10^{-3}	Shear rate, G (s^{-1})	Bending rigidity, EI (Nm^{2})	Viscous Flow Forcing (VFF) x 10^{3}
1 (short, low shear, type-A)	0.47	0.5	5.72×10^{-16}	0.0894
2 (short, high shear, type-A)	0.47	1.0	5.72×10^{-16}	0.1788
3 (short, low shear, type-B)	0.47	0.5	5.72×10^{-17}	0.8942
4 (short, high shear, type-B)	0.47	1.0	5.72×10^{-17}	1.788
5 (long, low shear, type-A)	0.58	0.5	5.72×10^{-16}	0.1744
6 (long, high shear, type-A)	0.58	1.0	5.72×10^{-16}	0.3489
7 (long, low shear, type-B)	0.58	0.5	5.72×10^{-17}	1.744
8 (long, high shear, type-B)	0.58	1.0	5.72×10^{-17}	3.489

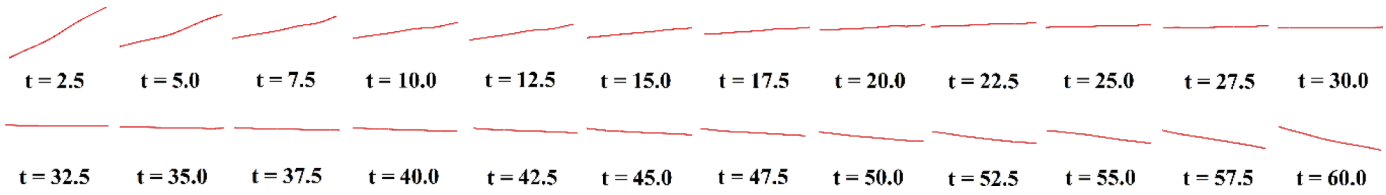

Fig. 27. Evolution of filament subjected to shear flow for $L = 0.25$, $K = 1.0$, $K_b = 1 \times 10^{-4}$ (***Re* = 0.875, VFF = 44.0**).

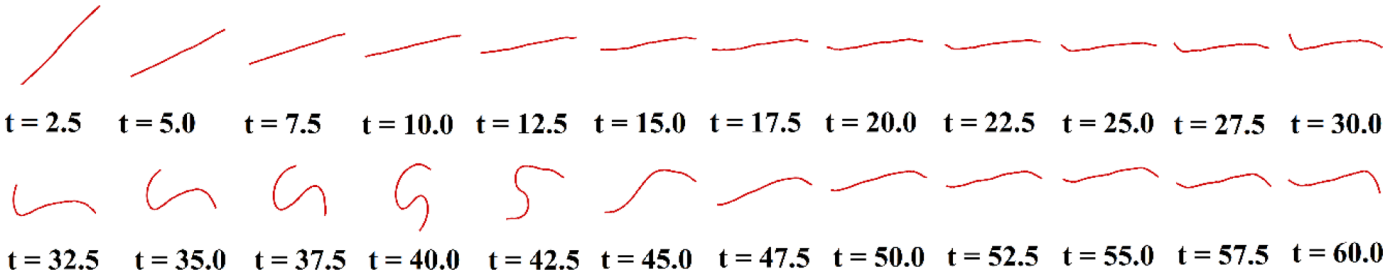

Fig. 28. Evolution of filament subjected to shear flow for $L = 0.25$, $K = 1.0$, $K_b = 1 \times 10^{-4}$ (***Re* = 8.0, VFF = 872.0**).

Table 6
Analysis factors such as symmetry breakage time, turning point time, deformation time and recurrence time calculated for all filament case conditions.

Case No. and condition (length, shear, recovery type)	Symmetry breakage time, t_{sb}	Turning point time, t_p	Deformation time, t_d	Recurrence time, t_r
1 (short, low shear, recuperative)	54.0	–	–	–
2 (short, high shear, recuperative)	22.0	26.0	4.0	22.5
3 (short, low shear, non-recuperative)	24.0	34.0	10.0	25.0
4 (short, high shear, non-recuperative)	7.5	15.0	7.5	11.0
5 (long, low shear, recuperative)	58.0	–	–	–
6 (long, high shear, recuperative)	30.0	34.0	4.0	22.0
7 (long, low shear, non-recuperative)	27.5	37.5	10.0	23.0
8 (long, high shear, non-recuperative)	10.0	17.5	7.5	7.4

ability to catch nutrients is lowered. Turning point time indicates the time for which the filament achieves a shape having the lowest end-to-end distance. It also helps to identify the highly deformed state of the filament. With reference to turning points, deformation time can be calculated. The deformation time indicates the ability of the initially deformed filament to reach its highly deformed state. Low deformation time indicates a faster recovery for the filament to reach undeformed position. Thus, the diatom can regain the undeformed state in a shorter period of time. Finally, recurrence time determines the frequency at which subsequent filament turning points occur. Smaller the recurrence time, higher is the turning point frequency. The filaments with high recurrence time tend to remain in the undeformed state longer. Therefore, the best possible condition is that filament must have high symmetry breakage time, low deformation time and high recurrence time (low recurrence frequency). However, these findings have never considered the role of nutrient uptake in diatom corresponding to diffusion, advection and chemical composition of diatom environment. The focus here is understanding the passive alignment of diatom chains based on an accurate representation of external turbulences or re-circulation zones in its vicinity.

The above-mentioned analysis factors for all cases are tabulated in Table 6 according to filament case conditions. The deformation time t_d is dependent on symmetry breakage time t_{sb}. When observing symmetry breakage time for all cases, it can be seen that $t_{sb} = 7.5$ for Case 4 which indicates that symmetry break occurs early for non-recuperative filaments subjected to higher shear rate. Short filaments break symmetry faster as compared to longer ones. Another observation when comparing filaments of the same length and same shear rate is that non-recuperative filaments break symmetry faster than recuperative filaments. Since non-recuperative filaments tend to bend the most, their end to end distance is also smaller. When observing filaments of the same length and same shear as in Case 2 and 4, the turning point time is

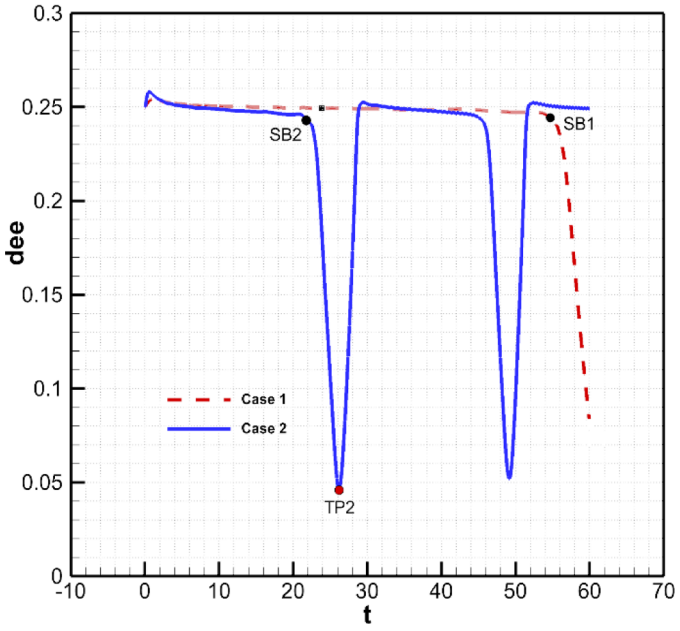

Fig. 29. Effect of d_{ee} with respect to time for varying shear rate (short recuperative filament).

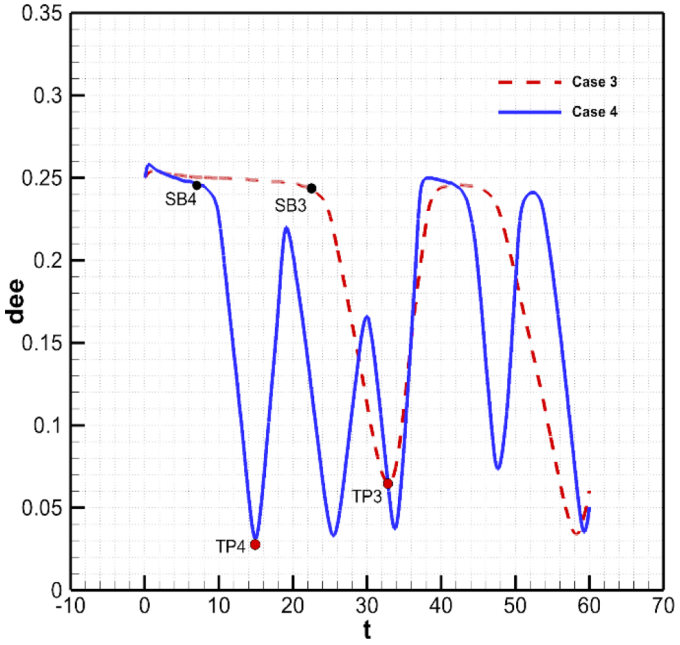

Fig. 30. Effect of d_{ee} with respect to time for varying shear rate (short non-recuperative filament).

small for non-recuperative filaments. Filaments subjected to lower shear rate also have higher turning points when compared with high shear filaments. The deformation time largely varies with respect to the shear rate as seen in case pairs corresponding to 2,4 and 6,8. The recurrence time t_r for all cases can be calculated by analyzing Figs. 29–32. Lower recurrence time indicates faster reproduction of turning points by the filament. Non-recuperative filaments which are placed in higher shear rates show higher recurrence rates at $t_r = 11.0$ for Case 4 (Table 6) and $t_r = 7.4$ for Case 8 (Table 6). Thus, non-recuperative filaments have a high frequency of recurrence. When comparing filaments based on length for fixed shear and rigidity, long filaments have higher symmetry breakage time, higher turning point time and lower recurrence time. This indicates that long filaments take less time to

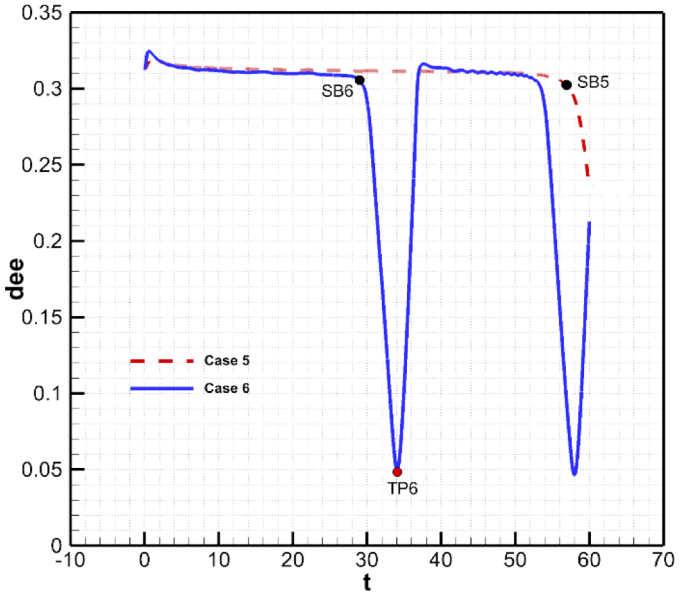

Fig. 31. Effect of d_{ee} with respect to time for varying shear rate (long recuperative filament).

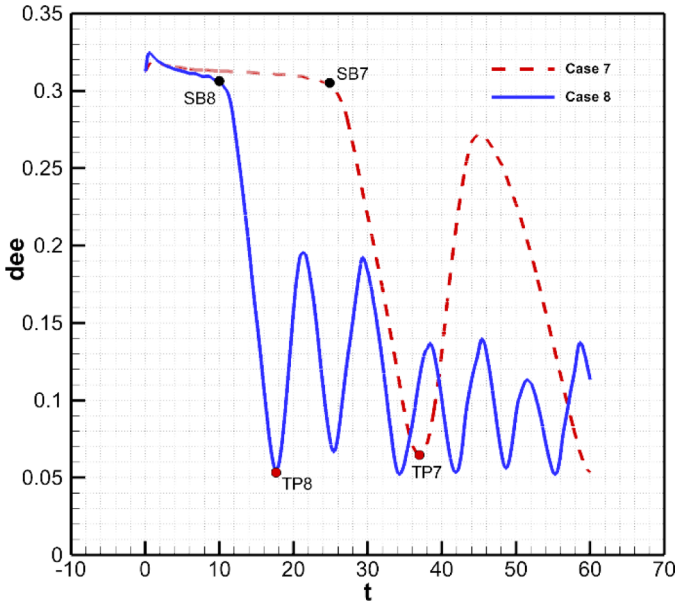

Fig. 32. Effect of d_{ee} with respect to time for varying shear rate (long non-recuperative filament).

achieve repeated turning behavior once the deformation is initiated. From the above discussion, the following ideal cases can be identified. Long recuperative filament subjected to low shear rate (high symmetry breakage time), Short and long recuperative filament placed in high shear rate (low deformation time) and Short non-recuperative filament in low shear flow (high recurrence time).

SB and TP with numeric case number notations are symmetry breaking points and turning points respectively which are indicated in all Figs. 29–32. The effect of varying shear rate on d_{ee} of short recuperative filaments is given in Fig. 29. The dotted line indicates filament subjected to lower shear rate and solid line for higher shear rates. A higher shear rate in Case 2 shows the lowest end to end distance, higher recurrence of turning points and faster symmetry breakage. In Fig. 30, the effect of shear rate on d_{ee} for short non-recuperative filaments is plotted for the simulation cycle. The recurrence of turning points is highest for non-recuperative filaments subjected to higher

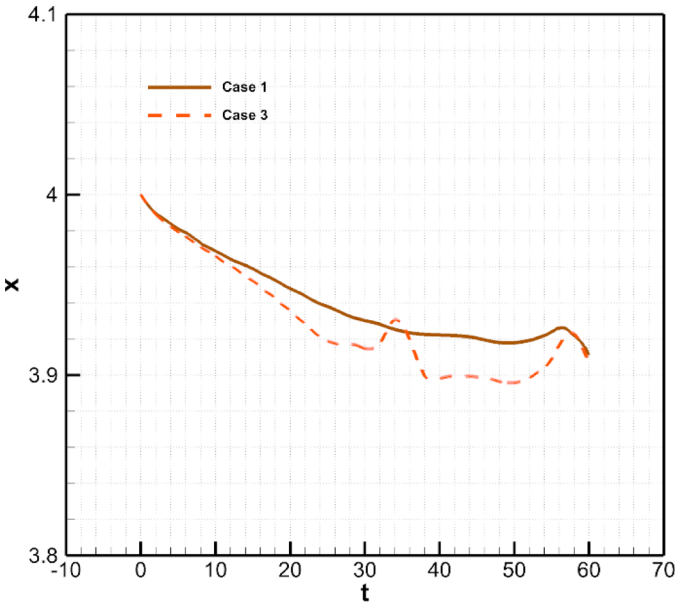

Fig. 33. Filament migration in the x-direction for varying bending rigidity (short filament in low shear flow).

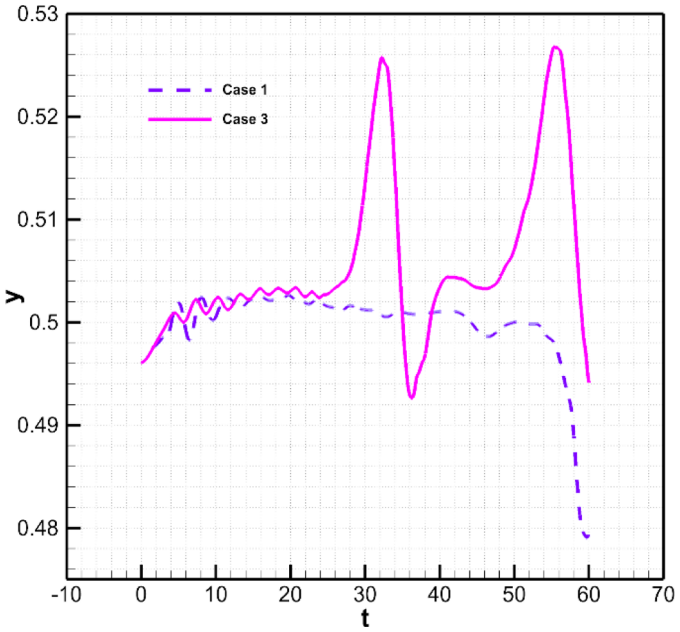

Fig. 34. Filament migration in the y-direction for varying bending rigidity (short filament in low shear flow).

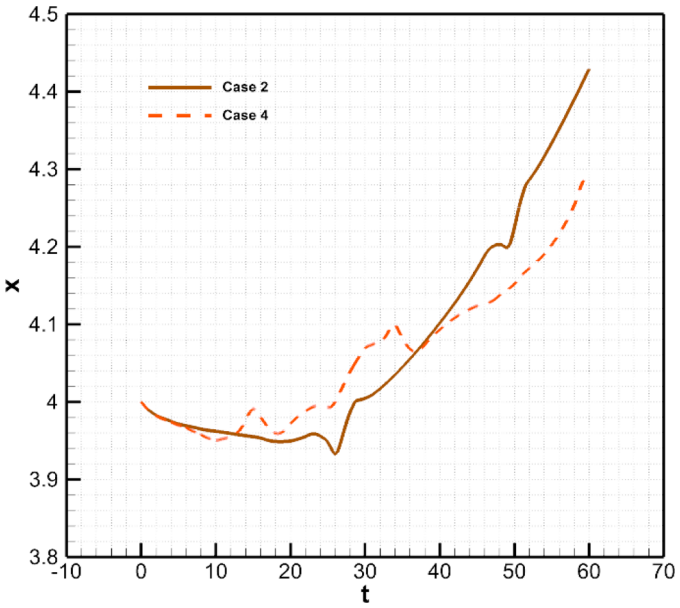

Fig. 35. Filament migration in the x-direction for varying bending rigidity (short filament in high shear flow).

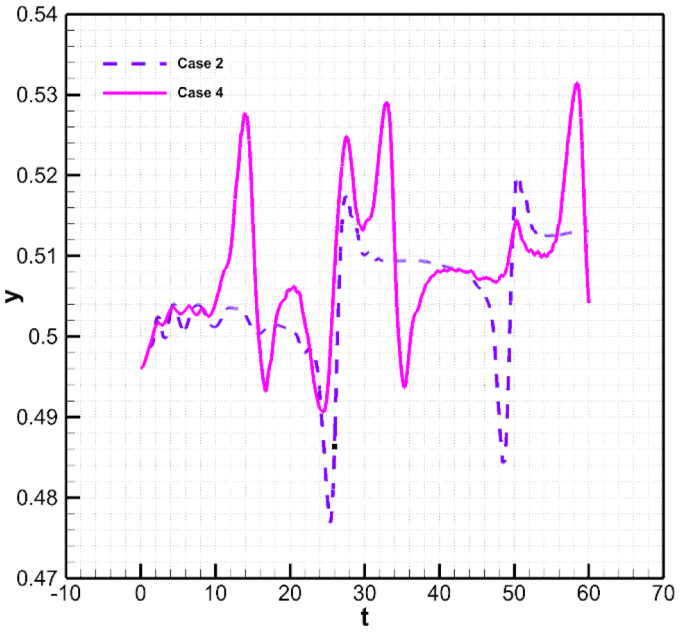

Fig. 36. Filament migration in the y-direction for varying bending rigidity (short filament in high shear flow).

shear rate with lower d_{ee}. The behavior of long filaments to different shear rate is plotted in Figs. 31 and 32 respectively. Fig. 31 also confirms that filaments at higher shear rate tend to deform faster which is shown by its early symmetry breakage and frequent recurrences within the simulation cycle. High recurrence frequency occurs for long non-recuperative filaments as seen in Fig. 32 (Case 8).

3.4. Filament migration

The fact that the filaments undergo deformation and turning for recuperative and non-recuperative cases prone to varying shear rates is well established in the previous section. We now focus on the migration and displacement produced by these filaments for various cases. The movement of the filament in the x-direction indicate its motion towards the entrance or exit of the channel and movement of the filament in the y-direction depicts motion towards upper or lower moving walls. The migration of short filaments subjected to lower shear rate with different bending rigidity in x-direction and y-direction is shown in Figs. 33 and 34 respectively. The filaments in Fig. 33 move towards the inlet irrespective of rigidity. However non-recuperative filament (Case 3) moves towards the top wall indicating that progression in shape causes a significant portion of the filament to move above the centerline (Fig. 34). Since recuperative filament (Case 1) has not achieved considerable deformation, it still remains below the centerline ($y = 0.5$). The maximum displacement in the x-direction with respect to channel midpoint (4.0, 0.5) is 0.1, and in the y-direction is 0.25. The same set of filaments are now subjected to higher shear rate as shown in Figs. 35 and 36 respectively. The deformation in the y-direction is similar to the

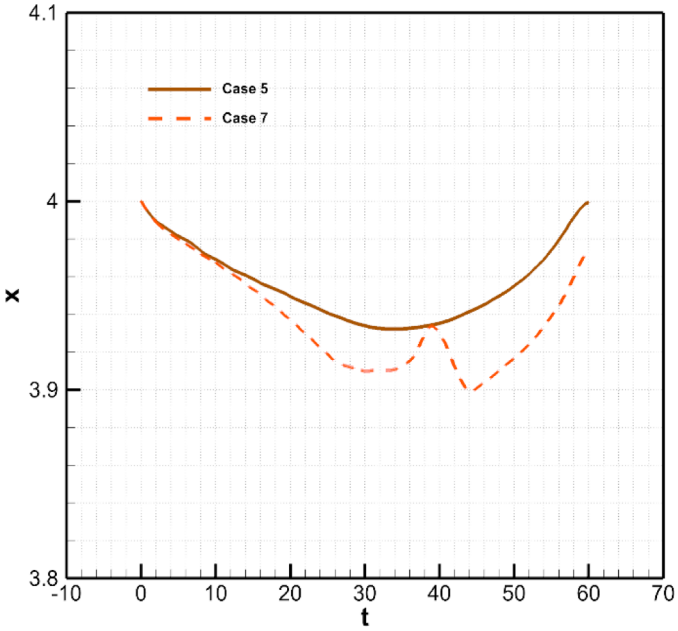

Fig. 37. Filament migration in the x-direction for varying bending rigidity (long filament in low shear flow).

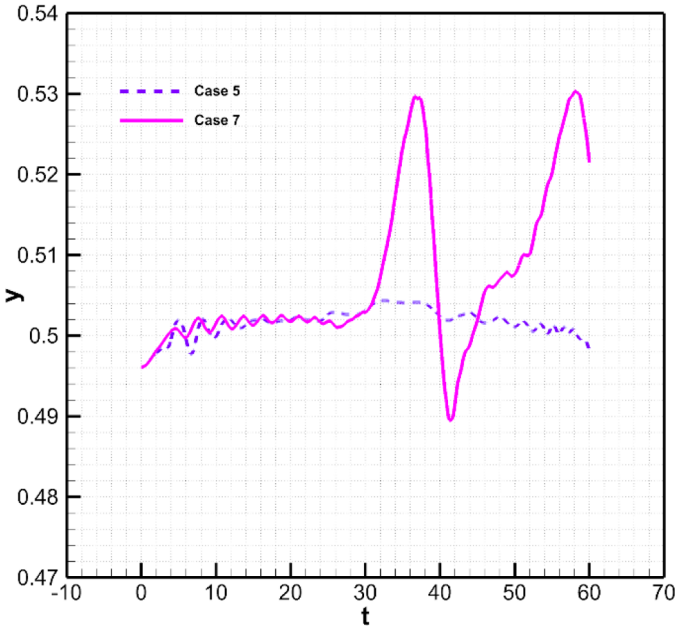

Fig. 38. Filament migration in the y-direction for varying bending rigidity (long filament in low shear flow).

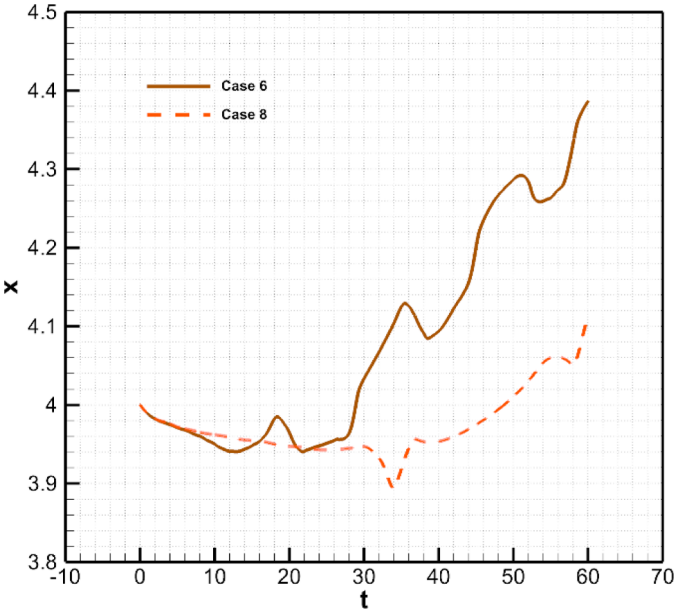

Fig. 39. Filament migration in the x-direction for varying bending rigidity (long filament in high shear flow).

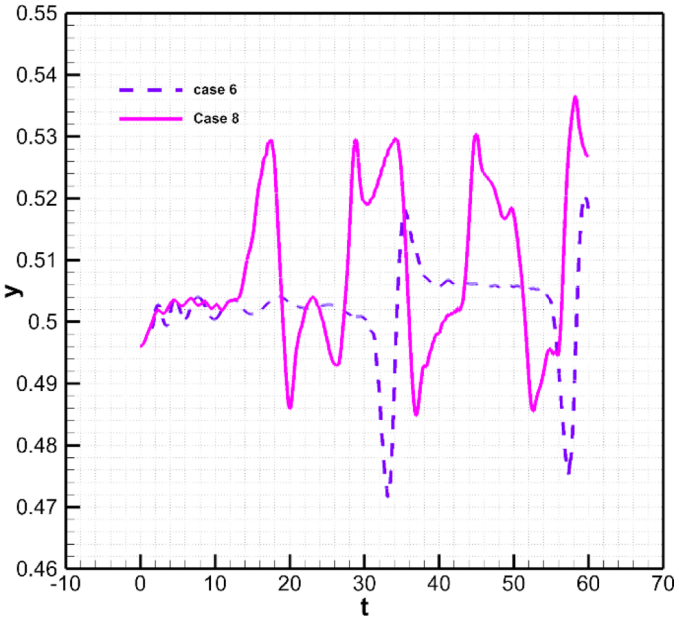

Fig. 40. Filament migration in the y-direction for varying bending rigidity (long filament in high shear flow).

previous case where recuperative filament (Case 2) tend to deform mostly below the centerline ($y = 0.5$) as seen in Fig. 36. The migration of both filaments (Case 2 and Case 4) is now shifted towards the exit of the channel with maximum displacement in x-direction being 0.42 and in y-direction 0.3 with respect to channel midpoint (4.0, 0.5). These displacements are higher when compared to low shear rate cases of Fig. 33 and Fig. 34, thus confirming that filaments at higher shear tend to be displaced the farthest. Figs. 37 and 38 show migration of long filaments of different bending rigidity subjected to lower shear rate. Both the filaments in Fig. 37 moves initially towards the inlet and returns back to the original position. In Fig. 38 non-recuperative filament (Case 7) move towards the top wall while the recuperative filament (Case 5) remains in the centerline position. The effective displacement in the x-direction is negligible whereas in the y-direction displacement is 0.3 with respect to channel midpoint (4.0, 0.5). When the same case is tested for higher shear rate, there is a drastic difference in x-direction displacement for recuperative and non-recuperative filaments as seen in Fig. 39. Recuperative filament (Case 6) is displaced the farthest when compared to non-recuperative (Case 8) towards the channel exit. The frequent occurrences of filament deformation cause the non-recuperative filament to migrate a short distance. The maximum displacement in the x-direction for this case is found to be 0.38. This displacement, when compared to that of short filament subjected to the same shear condition (Fig. 35, x-displacement = 0.42) is small, showing that short recuperative filament moves the farthest for all cases. The same behavior of short non-recuperative filament migrating above the centerline and recuperative filament moving below

centerline is also observed for long filaments in Fig. 40. Shear rate and flexibility have a significant contribution in deciding the direction of filament migration. Filaments subjected to higher shear rate tend to move towards the exit portion of the channel, and non-recuperative filaments move towards the top moving wall irrespective of the filament lengths considered in this study.

4. Conclusion

This study focuses on understanding the fluid-structure interaction of non-motile diatom chains subjected to shear flow in a viscous fluid medium having constant nutrition flux. The simulation is carried out in a two-dimensional manner by considering a flexible filament as a diatom placed in a channel. The interplay of hydrodynamics and filament properties like elasticity and bending are incorporated using an immersed boundary algorithm. The developed numerical model is validated by comparing with previous research works which involve deformation of a tethered flexible filament subjected to plane channel flow and un-tethered flexible filament in a planar shear flow at low Reynolds number. Further, the model is modified to incorporate a flexible filament mimicking a diatom chain placed in shear flow conditions. Filament shape deformations such as snake turns (C-shape) buckling and S-turns, documented by previous researchers are also observed in the present study. In this study, filament which retains their original shape after initial deformation is considered to be springy recuperative and those who do not retain shape are termed as non-recuperative. This is very important to determine how the diatom chain reacts to nutrients in their surrounding fluid and understand the passive alignment of diatom chains based on an accurate representation of external turbulences or recirculation zones in its vicinity. As observed from this study diatom that has Viscous Flow Forcing (VFF) in the range $0 < VFF < 350$ are considered to be recuperative and the ones having VFF beyond the value of 350 are non-recuperative. This helps us to identify the critical value of Viscous Flow Forcing (VFF) that govern the filaments ability to retain or attain permanent deformation from its original shape.

Based on the analysis of various factors such as symmetry breakage time, turning point time, deformation and recurrence time, optimum survival conditions for diatoms have been studied. Higher symmetry breakage time signifies that the filament remains in the undeformed state for a large portion of the time. This gives ample time for the filament to interact with the surrounding environment. In the case of diatom chains, it provides more time for it to absorb necessary nutrients. Low deformation time indicates a faster recovery for the filament to reach undeformed position. Thus, the diatom can regain the undeformed state in a shorter period of time. Finally, the filaments with high recurrence time tend to remain in the undeformed state longer. Therefore, the best possible condition is that filament must have high symmetry breakage time, low deformation time and high recurrence time (low recurrence frequency).

We found out the optimum survival conditions for the diatoms based on the above factor analysis. The present study indicates that long recuperative filaments subjected to low shear rate have high symmetry breakage time ($t_{sb} = 58.0$, Case 5), short and long recuperative filaments placed in high shear rate show low deformation time ($t_d = 4.0$, Case 2 and Case 6) and short non-recuperative filaments in low shear flow exhibit high recurrence time ($t_r = 25.0$, Case 3). Non-recuperative filaments subjected to high shear, usually tend to deform regularly due to high recurrence frequency ($t_r = 7.4$, Case 8 and $t_r = 11.0$, Case 4) which makes it challenging for the diatoms to collect nutrients. Filament migration study shows that short and recuperative filaments tend to migrate faster and deform less in shear flow, which is another critical observation of the behavior of the diatom chain to external flow conditions. The developed two-dimensional computational model based on the immersed boundary finite-volume method has been successful in capturing fluid dynamics near the filament surface and thus can be easily extended to study other non-motile biological organism interacting with surrounding fluid flow under different conditions.

Acknowledgments

This research was supported by Science and Engineering Research Board, a statutory body of Department of Science and Technology (DST), Government of India through the funded project ECR/2016/001501.

References

Batchelor, G.K., 1970. Slender-body theory for particles of arbitrary cross-section in Stokes flow. J. Fluid Mech. 44 (3), 419–440. https://doi.org/10.1017/S002211207000191X.

Bouzarth, E.L., Layton, A.T., Young, Y.N., 2011. Modeling a semi-flexible filament in cellular Stokes flow using regularized Stokeslets. Int. J. Num. Methods Biomed. Eng. 27 (12), 2021–2034. https://doi.org/10.1002/cnm.1454.

Dauptain, A., Favier, J., Bottaro, A., 2008. Hydrodynamics of ciliary propulsion. J. Fluids Struct. 24 (8), 1156–1165. https://doi.org/10.1016/j.jfluidstructs.2008.06.007.

Forgacs, O.L., Mason, S.G., 1959. Particle motions in sheared suspensions: X. Orbits of flexible threadlike particles. J. Colloid Sci. 14 (5), 473–491. https://doi.org/10.1016/0095-8522(59)90013-3.

Guasto, J.S., Rusconi, R., Stocker, R., 2012. Fluid mechanics of planktonic microorganisms. Ann. Rev. Fluid Mech. 44 (1), 373–400. https://doi.org/10.1146/annurev-fluid-120710-101156.

Hu, H.H., Patankar, N.A., Zhu, M.Y., 2001. Direct numerical simulations of fluid–solid systems using the Arbitrary Lagrangian–Eulerian technique. J. Comput. Phys. 169 (2), 427–462. https://doi.org/10.1006/jcph.2000.6592.

Hua, H., Shin, J., Kim, J., 2014. Dynamics of a compound droplet in shear flow. Int. J. Heat Fluid Flow 50, 63–71. https://doi.org/10.1016/j.ijheatfluidflow.2014.05.007.

Hayase, T., Humphrey, J.A.C., Greif, R., 1992. A consistently formulated QUICK scheme for fast and stable convergence using finite-volume iterative calculation procedures. J. Comput. Phys. 98 (1), 108–118. https://doi.org/10.1016/0021-9991(92)90177-Z.

Huang, W.X., Shin, S.J., Sung, H.J., 2007. Simulation of flexible filaments in a uniform flow by the immersed boundary method. J. Comput. Phys. 226 (2), 2206–2228. https://doi.org/10.1016/j.jcp.2007.07.002.

Jeffery, G.B., 1922. The motion of ellipsoidal particles immersed in a viscous fluid. Proc. R. Soc. London. Series A 102 (715), 161–179. https://doi.org/10.1098/rspa.1922.0078.

Jendrejack, R.M., Schwartz, D.C., De Pablo, J.J., Graham, M.D., 2004. Shear-induced migration in flowing polymer solutions: simulation of long-chain DNA in microchannels. J. Chem. Phys. 120 (5), 2513–2529. https://doi.org/10.1063/1.1637331.

Jumars, P.A., Trowbridge, J.H., Boss, E., Karp-Boss, L., 2009. Turbulence-plankton interactions: a new cartoon. Marine Ecol. 30 (2), 133–150. https://doi.org/10.1111/j.1439-0485.2009.00288.x.

Keller, J.B., Rubinow, S.I., 1976. Slender-body theory for slow viscous flow. J. Fluid Mech. 75 (4), 705–714. https://doi.org/10.1017/S0022112076000475.

Kim, B., Chang, C.B., Park, S.G., Sung, H.J., 2015. Inertial migration of a 3D elastic capsule in a plane Poiseuille flow. Int. J. Heat Fluid Flow 54, 87–96. https://doi.org/10.1016/j.ijheatfluidflow.2015.04.006.

Kim, B., Park, S.G., Huang, W.X., Sung, H.J., 2017. An autonomous flexible propulsor in a quiescent flow. Int. J. Heat Fluid Flow 68, 151–157. https://doi.org/10.1016/j.ijheatfluidflow.2017.10.006.

Kim, B., Park, S.G., Huang, W., Sung, H.J., 2016. Self-propelled heaving and pitching flexible fin in a quiescent flow. Int. J. Heat Fluid Flow 62, 273–281. https://doi.org/10.1016/j.ijheatfluidflow.2016.10.004.

Kunhappan, D., Harthong, B., Chareyre, B., Balarac, G., Dumont, P.J.J., 2017. Numerical modeling of high aspect ratio flexible fibers in inertial flows. Phys. Fluids 29 (9), 093302. https://doi.org/10.1063/1.5001514.

Karp-Boss, L., Boss, E., Jumars, P.A., 1996. Nutrient fluxes to planktonic osmotrophs in the presence of fluid motion. Oceanograp. Marine Biol. 34, 71–108.

Lindström, S.B., Uesaka, T., 2009. A numerical investigation of the rheology of sheared fiber suspensions. Phys. Fluids 21 (8), 083301. https://doi.org/10.1063/1.3195456.

Lindström, S.B., Uesaka, T., 2007. Simulation of the motion of flexible fibers in viscous fluid flow. Phys. Fluids 19 (11), 113307. https://doi.org/10.1063/1.2778937.

Lazier, J.R.N., Mann, K.H., 1989. Turbulence and the diffusive layers around small organisms. Deep Sea Res. Part A. Oceanograph. Res. Papers 36 (11), 1721–1733. https://doi.org/10.1016/0198-0149(89)90068-X.

Lai, M.C., Peskin, C.S., 2000. An immersed boundary method with formal second-order accuracy and reduced numerical viscosity. J. Comput. Phys. 160 (2), 705–719. https://doi.org/10.1006/jcph.2000.6483.

Liu, Y., Chakrabarti, B., Saintillan, D., Lindner, A., du Roure, O., 2018. Morphological transitions of elastic filaments in shear flow. Proc. Natl. Acad. Sci. 115 (38), 9438–9443. https://doi.org/10.1073/pnas.1805399115.

Maniyeri, R., Suh, Y.K., Kang, S., Kim, M.J., 2012. Numerical study on the propulsion of a bacterial flagellum in a viscous fluid using an immersed boundary method. Comput. Fluids 62, 13–24. https://doi.org/10.1016/j.compfluid.2012.03.012.

Maniyeri, R., Kang, S., 2012. Numerical study on the rotation of an elastic rod in a viscous fluid using an immersed boundary method. J. Mech. Sci. Technol. 26 (5), 1515–1522. https://doi.org/10.1007/s12206-012-0312-z.

Mittal, R., Iaccarino, G., 2005. Immersed boundary methods. Ann. Rev. Fluid Mech. 37 (1), 239–261. https://doi.org/10.1146/annurev.fluid.37.061903.175743.

Musielak, M.M., Karp-Boss, L., Jumars, P.A., Fauci, L.J., 2009. Nutrient transport and acquisition by diatom chains in a moving fluid. J. Fluid Mech. 638, 401–421. https://doi.org/10.1017/S0022112009991108.

Maniyeri, R., Kang, S., 2014. Numerical study on bacterial flagellar bundling and tumbling in a viscous fluid using an immersed boundary method. Appl. Math. Modell. 38 (14), 3567–3590. https://doi.org/10.1016/j.apm.2013.11.059.

Nguyen, H., Fauci, L., 2014. Hydrodynamics of diatom chains and semiflexible fibres. J. R. Soc. Interface 11 (96), 20140314. https://doi.org/10.1098/rsif.2014.0314.

Peskin, C.S., 2002. The immersed boundary method. Acta numerica 11, 479–517. https://doi.org/10.1017/S0962492902000077.

Ross, R.F., Klingenberg, D.J., 1997. Dynamic simulation of flexible fibers composed of linked rigid bodies. J. Chem. Phys. 106 (7), 2949–2960. https://doi.org/10.1063/1.473067.

Ryu, J., Park, S.G., Sung, H.J., 2018. Flapping dynamics of inverted flags in a side-by-side arrangement. Int. J. Heat Fluid Flow 70, 131–140. https://doi.org/10.1016/j.ijheatfluidflow.2018.02.009.

Shelley, M.J., Ueda, T., 2000. The Stokesian hydrodynamics of flexing, stretching filaments. Physica D 146 (1–4), 221–245. https://doi.org/10.1016/S0167-2789(00)00131-7.

Słowicka, A.M., Wajnryb, E., Ekiel-Jeżewska, M.L., 2015. Dynamics of flexible fibers in shear flow. J. Chem. Phys. 143 (12), 124904. https://doi.org/10.1063/1.4931598.

Stockie, J.M., Green, S.I., 1998. Simulating the motion of flexible pulp fibres using the immersed boundary method. J. Comput. Phys. 147 (1), 147–165. http://dx.doi.org/10.1006/jcph.1998.6086.

Shin, S.J., Chang, C.B., Sung, H.J., 2012. Simulation of a valveless pump with an elastic tube. Int. J. Heat Fluid Flow 38, 13–23. https://doi.org/10.1016/j.ijheatfluidflow.2012.08.003.

Stockie, J.M., 2002. Simulating the dynamics of flexible wood pulp fibres in suspension. In: Proceedings of the 16th Annual International Symposium on High Performance Computing Systems and Applications. IEEE Computer Society, pp. 154. http://doi.ieeecomputersociety.org/10.1109/HPCSA.2002.1019149.

Tornberg, A.K., Shelley, M.J., 2004. Simulating the dynamics and interactions of flexible fibers in Stokes flows. J. Comput. Phy. 196 (1), 8–40. https://doi.org/10.1016/j.jcp.2003.10.017.

Vanella, M., Posa, A., Balaras, E., 2014. Adaptive mesh refinement for immersed boundary methods. J. Fluids Eng. 136 (4), 040909.

Vahidkhah, K., Abdollahi, V., 2012. Numerical simulation of a flexible fiber deformation in a viscous flow by the immersed boundary-lattice Boltzmann method. Commun. Nonlinear Sci. Num. Simul. 17 (3), 1475–1484. https://doi.org/10.1016/j.cnsns.2011.07.039.

Wiens, J.K., Stockie, J.M., 2015. Simulating flexible fiber suspensions using a scalable immersed boundary algorithm. Comput. Methods Appl. Mech. Eng. 290, 1–18. https://doi.org/10.1016/j.cma.2015.02.026.

Yamamoto, S., Matsuoka, T., 1993. A method for dynamic simulation of rigid and flexible fibers in a flow field. J. Chem. Phys. 98 (1), 644–650. https://doi.org/10.1063/1.464607.

Young, A.M., Karp-Boss, L., Jumars, P.A., Landis, E.N., 2012. Quantifying diatom aspirations: mechanical properties of chain-forming species. Limnol. Oceanogr. 57 (6), 1789–1801. https://doi.org/10.4319/lo.2012.57.6.1789.

Zhu, L., Peskin, C.S., 2002. Simulation of a flapping flexible filament in a flowing soap film by the immersed boundary method. J. Comput. Phys. 179 (2), 452–468. https://doi.org/10.1006/jcph.2002.7066.